FEDERAL UNIVERSITY OF SANTA CATARINA
SCHOOL OF TECHNOLOGY
CHEMICAL ENGINEERING GRADUATE PROGRAM

Gabriela Xavier de Oliveira

CFD AND OPTICAL ANALYSIS OF A LUMINESCENT SOLAR CONCENTRATOR-BASED PHOTOMICROREACTOR

FLORIANÓPOLIS
2019

Gabriela Xavier de Oliveira

CFD AND OPTICAL ANALYSIS OF A LUMINESCENT SOLAR CONCENTRATOR-BASED PHOTOMICROREACTOR

Master thesis for the degree of Master in Chemical Engineering presented to the Graduate Program in Chemical Engineering at the Federal University of Santa Catarina.
Advisor: Prof. Dr. Cíntia Soares
Co-advisor: Prof. Dr. Natan Padoin
Prof. Dr. Timothy Noël

Florianópolis
2019

Ficha de identificação da obra elaborada pelo autor,
através do Programa de Geração Automática da Biblioteca Universitária da UFSC.

Xavier de Oliveira, Gabriela
CFD AND OPTICAL ANALYSIS OF A LUMINESCENT SOLAR CONCENTRATOR-BASED PHOTOMICROREACTOR / Gabriela Xavier de Oliveira ; orientador, Cíntia Soares, coorientador, Natan Padoin, coorientador, Timothy Noël, 2019.
96 p.

Dissertação (mestrado) - Universidade Federal de Santa Catarina, Centro Tecnológico, Programa de Pós-Graduação em Engenharia Química, Florianópolis, 2019.

Inclui referências.

1. Engenharia Química. 2. Computational Fluid dynamics (CFD). 3. Ray-tracing simulation. 4. Photomicroreactor. 5. Feedforward control. I. Soares, Cíntia . II. Padoin, Natan. III. Noël, Timothy IV. Universidade Federal de Santa Catarina. Programa de Pós-Graduação em Engenharia Química. V. Título.

Gabriela Xavier de Oliveira

CFD AND OPTICAL ANALYSIS OF A LUMINESCENT SOLAR CONCENTRATOR-BASED PHOTOMICROREACTOR

O presente trabalho em nível de mestrado foi avaliado e aprovado por banca examinadora composta pelos seguintes membros:

Prof.ª Claudia Sayer, Dr.ª
Universidade Federal de Santa Catarina

Prof. Bruno Augusto Mattar Carciofi, Dr.
Universidade Federal de Santa Catarina

Certificamos que esta é a **versão original e final** do trabalho de conclusão que foi julgado adequado para obtenção do título de mestre em Engenharia Química pelo Programa de Pós-Graduação em Engenharia Química da Universidade Federal de Santa Catarina.

Cintia Soares:02040162909
Digitally signed by Cintia Soares:02040162909
DN: cn=Cintia Soares:02040162909, o=ICPEdu, ou=UFSC - Universidade Federal de Santa Catarina
Date: 2019.08.20 12:53:13 -03'00'

Prof.ª Dr.ª Cíntia Soares
Coordenadora do Programa

Cintia Soares:02040162909
Digitally signed by Cintia Soares:02040162909
DN: cn=Cintia Soares:02040162909, o=ICPEdu, ou=UFSC - Universidade Federal de Santa Catarina
Date: 2019.08.20 12:53:25 -03'00'

Prof.ª Dr.ª Cíntia Soares
Orientadora

Florianópolis, 07 de junho de 2019.

This work is dedicated to my sources of strength, my parents and my grandmother.

ACKNOWLEDGEMENTS

First of all, I would like to express my gratefulness for being able to take a high-quality graduate course with highly qualified professors. Science in Brazil is a reality.

I thank my parents, whom I love immensely, without them none of this would be happening.

To my family, especially my brother, godmothers, and cousins. Thank you all for the affection and concern.

To my advisor, Prof. Cíntia Soares. Thank you for all the patience, support and commitment as professor and advisor. I am very proud to have been guided by you.

To my co-advisor, Prof. Natan Padoin. Thank you for your continued availability, your help was indispensable for this work.

Thanks to Prof. Timothy Noël and Dr. Dario Cambié for their attention and the information provided.

I also would like to thank my life friends, Priscila and Tairine. I know that I can always count on you both and I am very happy that we are always available to each other.

I also thank the great friends that I made in the masters, Ana Paula, Bernardo and Jessica, you guys are incredible.

A special thanks to all the members of the LabMAC group for all the happy moments I had in this lab.

Finally, I am thankful to CAPES (Coordination for the Improvement of Higher Education Personnel) and CNPq (National Council for Scientific and Technological Development) for financial support.

“...not all those who wander are lost...”
(J.R.R Tolkien, 1954)

RESUMO

A sustentabilidade nos processos é uma questão que vem sendo alvo de muita discussão ao longo dos anos. Uma nova tecnologia que emprega esse processo limpo é o foto microrreator baseado na tecnologia de concentrador solar luminescente (LSC-PM), o qual utiliza a luz do sol para promover reações químicas. Neste estudo, um modelo em CFD foi desenvolvido para a simular a conversão de 9,10-difenilantraceno (DPA) no LSC-PM. Os resultados simulados foram comparados com os dados experimentais de conversão de DPA em função do tempo para diferentes potências, com boa concordância. Três funções (retangular, triangular e sinusoidal) foram criadas para representar a variação temporal da potência. Um sistema de controle *feedforward* foi implementado no sistema de reação para manter uma conversão de DPA estável mesmo com as variações de irradiação ao longo do tempo. O estudo do tempo de atraso no sistema de controle foi feito com quatro tempos de atraso, 0,5, 1, 5 e 10 s, onde foi verificado que o atraso de 0,5 s resulta em controle em tempo real e é perfeitamente realizável. Além disso, duas configurações geométricas diferentes foram construídas para avaliar a influência desse parâmetro sobre o desempenho do sistema. Simulações da distribuição de fótons no LSC-PM foram conduzidas com base no método de Monte Carlo, utilizando a luz do sol como fonte. O livre caminho médio das partículas luminescentes foi variado para encontrar a melhor resposta e a interferência do mesmo no sistema óptico. Ao analisar a potência que atinge a superfície do dispositivo e a potência de saída, um livre caminho médio de 1 mm foi considerado razoável e posteriormente foi adotado para todas as simulações. Este estudo permitiu observar a variação das perdas pela diminuição/aumento da concentração de partículas de corante. Uma alta concentração implica em auto-perdas, e uma concentração muito baixa em um aumento de transmissões. A potência que atinge o dispositivo pôde ser medida, sendo que 1,7771W foi medido no interior do sistema, enquanto 0,0183W foram coletados pela borda de saída. As perdas de transmissão puderam ser elucidadas através das medidas coletadas por uma placa fina instalada sob o foto microrreator, e provou que 0,058 W da potência perdeu-se por transmissão. Duas novas espessuras do fotomicroreator foram desenvolvidas, a fim de comprovar que a geometria interfere no comportamento óptico do sistema, possibilitando a realização de estudos adicionais futuramente visando melhorias no sistema. Baseado nisso, as duas novas geometrias mostraram que, ao diminuir a espessura do dispositivo, as perdas são ampliadas no sistema.

Palavras-chave: LSC-PM. CFD. Traçado de raios. Controle.

RESUMO EXPANDIDO

Introdução

A utilização desenfreada de combustiveis fósseis, a qual gera condições climáticas desfavoráveis em nível global, gera a necessidade de novas rotas energéticas. Dentre os recursos energéticos renováveis, a luz solar mostra-se uma excelente alternativa, uma vez que é abundante em vários lugares do mundo, diferentemente dos combustíveis fósseis, que são escassos. Um dos usos da luz solar para a geração de energia é o concentrador solar luminescente (LSC), tecnologia desenvolvida há mais de trinta anos atrás, durante a crise energética, e ainda amplamente empregada. O sistema funciona de um modo simples, onde os fótons, após penetrarem na superficie superior do dispositivo são presos no mesmo e reemitidos para as bordas da placa onde celulas fotovoltaicas são alocadas e resposáveis pela conversão em energia eletrica. Porém, não é apenas a industria energética que necessita de rotas mais sustentáveis. Estimulados pelo aumento dos processos limpos de geração de energia, os processos sustentáveis na industria química começaram a ganhar espaço. Os processos fotoquímicos, os quais em seus primórdios eram efetuados com luz solar, voltaram a repensar e reutilizar o uso da mesma. Com isso em mente, Cambié *et al*. (2017), propuseram um foto microrreator para promover reações químicas a partir de luz solar, o fotomicrorreator baseado na tecnologia de concentrador solar luminescente (LSC-PM). Tal foto microrreator constitiu-se em uma fusão sinérgica entre o LSC e microcanais, gerando um microrreator de baixo custo e simples, capaz de realizar sinteses químicas, o qual leva como reação de referência a cicloadição [4+2] de 9,10 difenilantraceno (DPA). Dentre as várias questões presentes quando se trabalha com luz solar, mudanças na irradiação solar durante o dia tornam-se um dos maiores desafios. Com isto em mente, Zhao, *et al*. (2018), implementaram um sistema de controle *feedforward* no LSC-PM, o qual foi responsável por manter a conversão constante independente das oscilações de irradiação durante o dia. Porém, apesar das variadas vantagens do LSC-PM, algumas desvantagens ainda estão presentes no sistema. Além das mudança da irradiação durante o dia já citadas, as perdas de energia do sistema e o fluxo de fótons atingindo os microcanais podem ser alguns dos fatores que interferem na eficiência do sistema. Simulações de traçados de raios e em CFD podem se tornar ferramentas capazes de elucidar e minimizar essas questões.

Objetivos

Tendo em vista que sistemas fotoquímicos apresentam perdas energéticas, simulações de traçados de raios podem ser realizadas nos sistemas. Deste modo, sugeriu-se a simulaçao de traçado de raios para quantificar as perdas energéticas do sistema e minimizá-las. Este trabalho visa também, implementar um modelo CFD do LSC-PM, simulando o sistema de controle visando primeiramente uma validação, para posterior otimização do sistema. Além de, avaliar a performance do LSC-PM com e sem o controle, variados tempos de atraso e com diferentes intensidades de luz. Novas geometrias foram propostas também para otimização da performance do foto microrreator.

Metodologia

A metodologia, assim como os resultados, dividiu-se em duas seções: (i) simulação em CFD; (ii) simulação de traçado de raios. O primeiro item, (i) simulação em CFD, foi efetuado no software COMSOL *Multiphysics*® (versão 5.3a). A metodologia deste item (i) seguiu as seguintes etapas: a) desenvolvimento da geometria do LSC-PM no COMSOL *Multiphysics*® com as dimensões originais; b) implementação do teste de independência de malha proposto por Celik *et al.* (2008).; c) determinação da constante de velocidade de pseudo-primeira ordem, através de dados fornecidos pelo Noël Research Group; d) após a validação do modelo computacional com o experimental, variações da intensidade de luz foram representadas através de distúrbios no software COMSOL *Multiphysics*® na forma sinusoidal, retangular e triangular; e) desenvolvimento do sistema *feedforward* de controle para manter a conversão constante independente da irradiação do dia. Para tal, foi necessário realizar um balanço de massa a fim de descobrir como a velocidade varia com a potência, utilizando como hipóteses: estado estacionário e *plug-flow* na direção x. f) variação do tempo de atraso a fim de verificar o comportamento do sistema; g) desenvolvimento de duas novas geometrias para minimizar a formação de zonas mortas no LSC-PM através da função *fillet* e elipse do COMSOL *Multiphysics*®. Quanto ao segundo item, (ii) simulação de traçado de raios, a metodologia deste tópico seguiu as seguintes etapas: a) implementar a geometria original do LSC-PM juntamente com as características ópticas no *software* LightTools®, definindo-se nesse caso, 100% absorção nas laterais, e "tipo Fresnel" no topo e base do reator; b) o próximo passo da metodologia tratou-se então do procedimento de dopagem de corante do sistema, onde o espectro de absorção e emissão (WIELAND, 2016), e o rendimento quântico (BASF, 1997) foram definidos no sistema; c) o livre caminho médio (MFP) devido à ausência de dados, foi assumido, utilizando um caso base citado por Chavéz *et al.* (2017); d) na modelagem da fonte de luz, considerou-se a data e as coordenadas originais da região onde os experimentos foram realizados, obtidos através dos dados suplementares de Zhao *et al*. (2018); e) após a inserção de todos os parâmetros, uma variação na espessura do foto microrreator foi feita de modo a observar a interferência da mesma na performance do sistema; f) receptores foram acoplados em três superfícies do foto microrreator para quantificar a potência atingindo o mesmo.

Resultados e Discussão

Na (i) simulação em CFD: os dados simulados apresentaram uma excelente concordância com os dados experimentais com um erro máximo <13%. Deste modo, pode ser estabelecido que o modelo simulado representa satisfatoriamente a conversão de DPA em diferentes intensidades de luz. Quando se diz respeito ao sistema do controle, observou-se que o sistema sem nenhum controle, não apresentou uma conversão constante, como era esperado. Pelo contrário, quando a irradiação diminuía, a conversão diminuía de mesmo modo (de~ 80% para < 10%). Ao aplicar o sistema de controle o comportamento oposto foi observado, onde o sistema de controle foi capaz de manter a conversão em torno de ~90% mesmo com as diferentes intensidades de luz. Quanto as três funções desenvolvidas para representar a intensidade de luz (triangular, sinusoidal e retangular) com diferentes tempos de atraso*:* 0,5, 1, 5 e 10 s, observou-se que a diferença de conversão entre os tempos de atraso de 0,1 e 1 é praticamente nulo. Diferentemente, o tempo de

atraso de 5 s demonstrou diferenças substanciais na conversão. Consequentemente, o tempo de atraso de 10 s foi o que mais demonstrou desvio do set-point. Dentre os distúrbios, a função triangular foi a que mais demonstrou um decaimento drástico com a diminuição da intensidade da luz. Comportamento que pode ser explicado devido ao fato de que quando ocorre uma diminuição repentina da intensidade da luz, sem uma diminuição imediata da vazão, o resultado é uma diminuição da taxa de reação e consequentemente na conversão. Com a mudança das geometrias, observou-se que com a geometria elipse obteve-se a maior conversão 91,27%, quando comparada a conversão da geometria original, 90,67%. A geometria *fillet* resultou em uma conversão de 90,96%, não tão diferente do desempenho obtido com a geometria original. Deste modo, a geometria original, mesmo com suas extremidades retangulares, apresentou comportamento aceitável quando comparado as duas novas geometrias, não demonstrando necessidade de substituição. Na (ii) simulação de traçado de raios: algumas perdas foram elucidadas, onde, 1,771 W foram coletados incidindo a superfície do reator, e apenas, 0,117 W foram absorvidos pelos microcanais. Sendo que, 0,058 W foram perdidos por transmissão dos 0,117 W totais. A potência de saída também foi coletada visando uma futura validação com os dados de Zhao *et al.* (2018), onde encontrou-se um valor de 0,00183 W atingindo as laterais (saída), ou seja, apenas uma porcentagem de 7,39% dos raios acaba por atingir as laterais do reator (considerando 100% de absorção). O livre caminho médio (MFP) foi então avaliado, o qual era desconhecido. Através de intervalos que variavam de $0{,}1-20\text{mm}$, encontrou-se o valor ideal de $\text{MFP}\approx 1\text{mm}$. Onde este valor foi escolhido devido ao fato de que com valores muito altos de MFP observou-se que ocorria diminuições na potência absorvida e na potência de saída do reator, o que é causado pelo alto índice de transmissão. E valores muito baixos de MFP geravam também concentrações muito altas de corante no sistema, ocasionando muitas perdas por auto-absorção. A modificação da espessura da geometria mostrou um resultado promissor para futuros estudos, representando que tal fator influencia na eficiência do sistema tanto na fluidodinâmica quanto na performance óptica. Conforme aumentou-se a espessura do reator, houve também, de mesmo modo, um leve aumento na potência absorvida e na potência de saída.

Considerações Finais

Este estudo destacou que a ferramenta de CFD pode ser aplicada com sucesso na investigação da fluidodinâmica em um microrreator. O modelo de CFD desenvolvido mostrou boa concordância com os dados experimentais, possibilitando a validação do modelo. O sistema *feedforward* implementado no sistema de reação foi capaz de manter a conversão no valor alvo apesar das mudanças da irradiação de luz. Além disso, a geometria original mostrou bom comportamento quando a conversão foi estudada, não havendo necessidade de alteração. A partir da simulação óptica, foi possível elucidar a potência que atinge o sistema. A potência que atinge a parte superior do dispositivo e a potência de saída também puderam ser coletadas. A investigação das perdas provou que estudos a respeito da otimização ainda podem ser feitos para melhorar o desempenho do sistema (*e.g.* otimização da geometria). A validação é o próximo passo principal, tendo em vista que, para fazer a otimização, as simulações devem ter um bom acordo com os dados experimentais.

Palavras-chave: LSC-PM. CFD. Traçado de Raios. Controle.

ABSTRACT

Process sustainability is a question that has attracted significant attention in the last decades. A novel technology that employs this clean process is the luminescent solar concentrator-based photomicroreactor (LSC-PM), a microreactor that utilizes sunlight to drive chemical reactions. In this study, a CFD model was built for the simulation of the conversion of 9,10-diphenylanthracene (DPA) in the LSC-PM. The numerical results were compared with the experimental data of DPA conversion *versus* time for different powers, and the agreement was quite satisfactory. Three functions (rectangular, triangular and sinusoidal) were created in order to represent the temporal variation of the power. A feedforward control system was implemented in the reaction system in order to maintain a stable DPA conversion due to power variations over time. The study of the time delay in the control system was made with four levels, 0.5, 1.5 and 10 s, where it was verified that, in fact, a 0.5 s delay resulted in a realizable real-time control. Furthermore, the influence of different geometrical configurations for the microchannels on the reactive flow was investigated. Moreover, optical simulations were carried out to quantify the photon distribution in the system based on Monte Carlo method. These ray-tracing simulations used sunlight as a source. The mean free path (MFP) of the luminescent particles was variated in order to find the best response and the interference of this parameter on the performance of the optical system. When analyzing the power that reaches the device and the output power, a 1 mm MFP was considered adequate and adopted for all the simulations. This study allowed the observation of the variation of losses by the decrease/increase of the concentration of dye particles. A high concentration implies in self-losses, while a very low concentration implies in higher transmissions. The power attaching the device by sunlight irradiation could be measured, where 1.7771 W was found impinging in the system, while 0.0183 W was collected by the output edge. The transmission losses could be elucidated by attaching a thin plate under the photomicroreactor, and it proved that 0.058 W of the power was lost by transmission. Two new thickness of the photomicroreactor were evaluated, in order to prove that it interferes in the optical behavior of the system, allowing further improvement studies on the system. These two new dimensions showed that by decreasing the thickness of the device the losses are consequently increased.

Keywords: LSC-PM. Ray-tracing. CFD. Control.

LIST OF FIGURES

LIST OF TABLES

LIST OF ABBREVIATIONS

CFD	Compututional Fluid Dynamics
DPA	Diphenylanthracene
ESA	Excited State Absorption
GCI	Grid Convergence Index
IAE	Integral Absolute Error
IC	Internal Conversion
ISC	Internal System Crossing
ISE	Integral Square Error
ITAE	Integral of time multiplied absolute error
LEDs	Light-Emitting Diodes
LSC	Luminescent Solar Concentrator
LSC-PM	Luminescent Solar Concentrator Photomicroreactor
MB	Methylene Blue
MFP	Mean Free Path
PDMS	Polydimethylsiloxane
PFA	Perfluoroalkoxyalkane
PMMA	Polymethylmethacrylate
PV	Photovoltaic
SET	Single Electron Transfer
TIR	Total Internal Reflection
UV	Ultraviolet

LIST OF SYMBOLS

$\upsilon_x, \upsilon_y, \upsilon_z$	velocity components $(\mathrm{m} \cdot \mathrm{s}^{-1})$
C_i	concentration of specie *i* $(\mathrm{mol} \cdot \mathrm{m}^{-3})$
$C_{i,0}$	initial concentration of specie *i* $(\mathrm{mol} \cdot \mathrm{m}^{-3})$
k	rate constant (s^{-1})
$F_{i,0}$	molar feed rate $(\mathrm{mol} \cdot \mathrm{s}^{-1})$
X	conversion $(\%)$
V	volume of reactor (m^3)
P	power (W)
τ	space time (s)
$\dot{Q}$	volumetric rate $(\mathrm{m}^3 \cdot \mathrm{s}^{-1})$
A	area (m^2)
ρ	density $(\mathrm{kg} \cdot \mathrm{m}^{-3})$
P	pressure (Pa)
τ_{ij}	component of stress tensor
μ_i	dynamic viscosity for each species *i* in the mixture $(\mathrm{Pa} \cdot \mathrm{s})$
x_i	mole fraction of specie *i*
$\vec{n}$	normal velocity
$\vec{t}$	tangential velocity
$J_{i\,(x,y,z)}$	molecular diffusion flux of the species in *x*,*y*,*z* direction $(\mathrm{mol} \cdot \mathrm{m}^{-2} \cdot \mathrm{s}^{-1})$
$D_{i,m}$	molecular diffusion coefficient for specie *i* in the mixture $(\mathrm{m}^2 \cdot \mathrm{s}^{-1})$
D_{ij}	molecular diffusion coefficient for the pair *i-j* $(\mathrm{m}^2 \cdot \mathrm{s}^{-1})$
ϕ_j	association parameters
T	absolute temperature (K)
$M_{w,j}$	molecular weight $(\mathrm{g} \cdot \mathrm{mol}^{-1})$
$^1O_2$	singlet oxygen
T	transmission

α	absorption coefficient
λ	wavelength (nm)
$\alpha(\lambda)$	absorption spectrum
k	extinction coefficient
n	refractive index

CONTENTS

1 INTRODUCTION

1.1 MOTIVATION

Among renewable energy resources, solar light is an excellent alternative, given that it is eco-friendly, free and abundant in several places around the world, unlike fossil fuels that are finite (KABIR *et al.*, 2018; LEELADHAR; RATURI; SINGH, 2018; SANSANIWAL; SHARMA; MATHUR, 2018; YADAV *et al.*, 2018). The use of solar energy requires capture, solar conversion and storage, and currently, is widely used for the generation of heat and electricity (LEWIS; NOCERA, 2006; SCHOLES *et al.*, 2011).

About more than 30 years ago, during the energy crisis, a technology was proposed aiming at concentrating solar energy for electricity production, the so-called luminescent solar concentrators (LSCs) (DEBIJE, 2010; MEINARDI; BRUNI; BROVELLI, 2017; MORAITIS; SCHROPP; VAN SARK, 2018). The LSCs operate through the light penetration on the upper surface of the device where re-emission of absorbed photons occurs. Afterward, this light is concentrated along the edges of the plate where it is collected by small photovoltaic cells responsible for converting it in electrical energy (DEBIJE; VERBUNT, 2012; MORAITIS; SCHROPP; VAN SARK, 2018; SARK *et al.*, 2008).

Recently, solar energy has also been used for the synthesis of chemical compounds, since the introduction of sunlight-driven photocatalysis (OELGEMÖLLER, 2016; SCHOLES *et al.*, 2011; SCHULTZ; YOON, 2014). Inspired by the LSC technology, a novel luminescent solar concentrator-based photomicroreactor (LSC-PM) was developed at the Noël research group (http://www.noelresearchgroup.com/), Eindhoven University of Technology, The Netherlands, to promote fast chemistry under sunlight irradiation (CAMBIÉ *et al.*, 2017a; ZHAO *et al.*, 2018b). This microreactor is composed by a synergistic combination of luminescent solar concentrators and microchannels, allowing simple and inexpensive reactors, which

enables the efficient use of sunlight for photochemical transformations (CAMBIÉ *et al.*, 2017b).

In addition, the use of microreactors has unique advantages for photochemical reactions, since it merges the small dimensions of the devices with the continuous flow mode (OELGEMÖLLER, 2012). Continuous flow operation presents a significant reduction in solvent requirements, ensuring sufficient light penetration (ODIBA *et al.*, 2016), under totally customizable designs. Moreover, this operation mode is preferred for the synthesis of added-value compounds such those used in the pharmaceutical industry as active agents or intermediates given the excellent controllability, ensuring high quality for the chemicals synthesized.

However, despite all the reported advantages of the LSC-PM, there is still plenty of room for improvements, especially when one considers the modeling of photon distribution in the device and its coupling with the reactive flow taking place in the microchannels. The leakage of the photons when the irradiation impinges in the domain is a clear example. In this context, ray-tracing methods have been used as an effective tool to quantify photon losses and optimize the system, allowing to track the photon fate taking into account the effect of the optical properties of surfaces, materials and emission sources (KERROUCHE *et al.*, 2014). This information is of paramount importance to minimize energy losses and intensify the photon flux reaching the microchannels, resulting in enhanced reaction rates.

Additionally, when sunlight is considered, one has to figure out the effect of fluctuations in the irradiation along the day, which impose a real challenge for this technology. An efficient alternative to overcome this problem has been recently reported, based on real-time feedforward control of the system, maintaining a constant conversion regardless of the light intensity that reaches the device during the day (ZHAO *et al.*, 2018). CFD techniques can provide important insights about the behavior of microreactors, allowing to investigate control strategies as well as the effect of different geometrical configurations and operating conditions on the device's performance (ODIBA *et al.*, 2016), highlighting flow non-idealities for instance. Thus, once validated, a CFD model is a powerful tool for the optimization of photomicroreactors seeking for effective scale-out of the system.

Given this context, this work aims to implement a CFD model of a LSC-PM device applied to the cycloaddition of 9,10-diphenylanthracene (DPA), took as benchmark reaction (CAMBIÉ *et al.*, 2017b), and numerically investigate a feedforward control strategy. In addition, it also intends to quantify the energy losses of the device exposed to sunlight irradiation through ray-tracing simulations.

1.2 OBJECTIVES

1.2.1 General objective

The general objective of this work is to investigate the 9,10-diphenylanthracene (DPA) synthesis in an LSC-PM under fluctuating solar irradiation by CFD, subjected to a feedforward control strategy, and implement a ray-tracing model to quantify energy losses in the device.

1.2.2 Specific objectives

To meet the general objective presented at item 1.2.1, this work is based on the following specific goals:

- obtain a light-dependent kinetic model for the cycloaddition of 9,10-diphenylanthracene (DPA) in an LSC-PM.
- validate a CFD model with experimental data available in the literature.
- evaluate the performance of the LSC-PM under different light intensities.
- compare the efficiency of the LSC-PM with/without a control system.
- observe the response of the control system with different time delays.
- propose new geometries for the improvement of the LSC-PM's performance.
- quantify the energies losses in the microreactor.
- analyze the photon fate when sunlight irradiation reaches the LSC-PM.

2 THEORETICAL BACKGROUND

2.1 SUNLIGHT

Clean energy is an environmental question that is gaining more space over the years. Considering that the release of carbon dioxide and greenhouse gases is deeply harmful to the environment and that the depletion of the oil reserves is at alarming levels, the quest for alternative energy sources is a central point for future technological development (OBAMA, 2017; SANSANIWAL; SHARMA; MATHUR, 2018). Among renewable energy resources, sunlight is an excellent alternative, once it is eco-friendly, free and abundantly available in several places around the world (KABIR *et al.*, 2018; LEELADHAR; RATURI; SINGH, 2018; SANSANIWAL; SHARMA; MATHUR, 2018; YADAV *et al.*, 2018).

Given the excellent potential of this energy source, several researches have explored ways to harvest sunlight not only for electricity generation but also to drive photocatalyzed chemical reactions. Pohlmann *et al*. (1997) demonstrated the suitability of sunlight-driven chemical reactions using moderately concentrated irradiance (OELGEMÖLLER; JUNG; MATTAY, 2007). Several studies have been devoted to developing sunlight-driven chemistry since then (CAMBIÉ *et al.*, 2017a; OELGEMÖLLER, 2016; SCHOLES *et al.*, 2011; SCHULTZ; YOON, 2014).

The use of solar light as a source of photons for photocatalyzed reactions is a promising field, including applications in degradation of liquid and gas-phase pollutants, synthesis of advanced materials and synthesis of chemicals, especially added-value molecules.

2.2 PHOTOCHEMISTRY

Photochemistry is an important technological alternative for the synthesis of organic compounds (CIANA; BOCHET, 2007). Commonly, the photochemical reactions are induced by high-energy ultraviolet (UV) or visible photons, which are responsible for the necessary energy to produce molecular transformations

(MUKAMEL, 1997; SHVYDKIV, 2012). Max Planck, the father of quantum physics, theorized that this energy was transferred in parts, or quanta, equal to hv, expressed according to Equation (1) (KAOARNOS, 1993).

$$E = n \cdot hv \tag{1}$$

where E is the energy of the photon, h is Max Planck constant, v is frequency, and n is the number of photons.

Based on this theory, it is possible to say that molecules can exist in different electronic states, depending on the quantity of energy provided (WASSERBERG, 2006). These electronic states can be considered energetically unstable and chemically different from their corresponding ground states, with very brief life, around nanoseconds (RAZEGHIFARD, 2013). The possible transitions after the photoexcitation of a molecule are represented by the Jablonski diagram (Figure 1).

Figure 1 - Simplified Jablonski diagram.

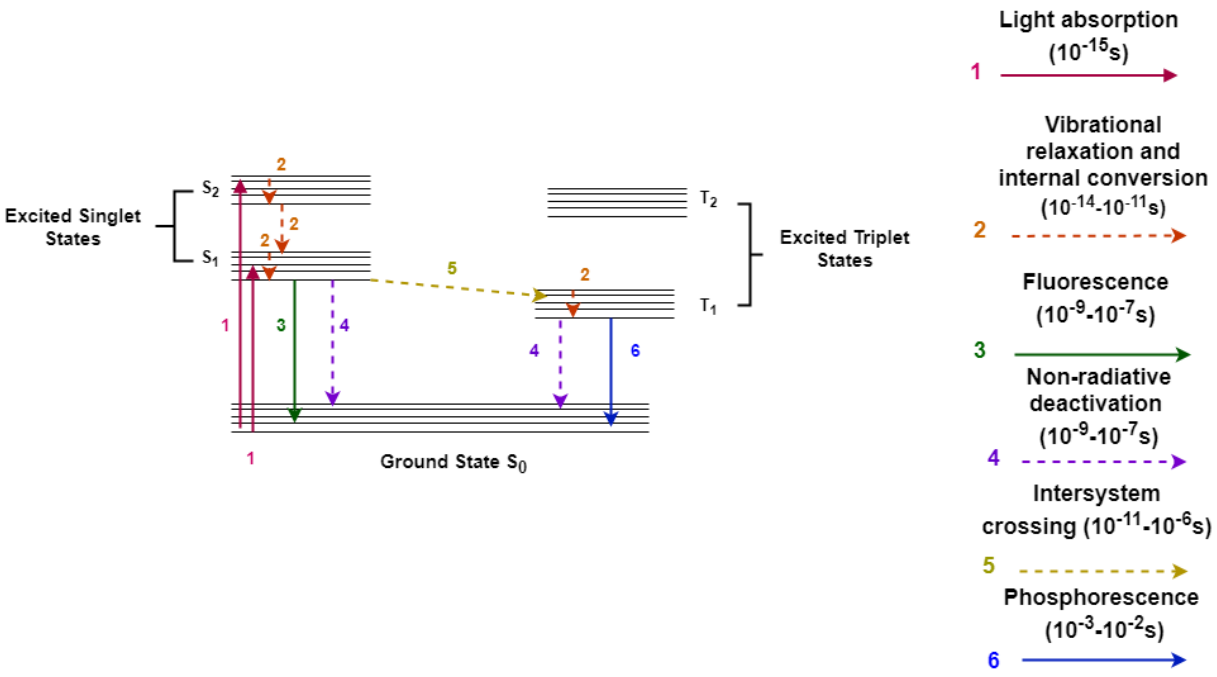

Reference: adapted from Razeghifard (2013).

These processes of transitions (Figure 1) can be explained as follows (WASSERBERG, 2006):

1. So ground state: corresponds to the state of the molecule prior do the photon absorption.

2. $So + h\nu \rightarrow S_1$ singlet-singlet absorption: after the photoexcitation of the molecule, it is elevated from the ground state to a higher energy level, reaching the S_1 state.

3. $So + 2\,h\nu \rightarrow S_1$ two-photon singlet-singlet absorption: as the name indicates, two photons are absorbed by a molecule that is in the ground state, and almost simultaneously the molecule is elevated to the S_1 state.

4. $So + h\nu \rightarrow T_1$ singlet-triplet absorption: occurs when a photon absorbed does not contain sufficient energy to excite the molecule to the S_1 state; however, it is able to excite the molecule to the triplet state.

5. $T_1 + h\nu \rightarrow T_n$ triplet-triplet absorption: occurs when a photon is absorbed by a molecule in T_1 excited state, generating an excitation to an even higher triplet state T_n. It can be characterized as a form of excited-state absorption (ESA).

6. $S_1 \rightarrow S_o + h\nu$ fluorescence: when a molecule in its excited singlet state decays radiatively between states of the same spin state. This can occur under the emission of a photon.

7. $T_1 \rightarrow S_o + h\nu$ phosphorescence: the molecule located in the excited triplet state emits a photon and come back to the singlet ground stated.

8. $S_1 \rightarrow S_0 + \Delta$ internal conversion (IC): happens when a molecule that $T_n \rightarrow T_1 + \Delta$ is in an excited state goes through another electronic state of the same spin multiplicity. Then, the nonradiative decay due to the loss of vibrational quanta results in a release of thermal energy (Δ).

9. $S_1 \rightarrow T_1 + \Delta$ intersystem crossing (ISC): when a molecule that is in $T_1 \rightarrow S_0 + \Delta$ an excited state goes through another electronic state with a different spin multiplicity. Then, the nonradiative decay due to the loss of vibrational quanta results in a release of thermal energy (Δ).

In these processes, the shorter wavelengths of the photons allow direct interaction with molecular bonds. For this reason, the performance with UV is better due to its wavelength, $\lambda < 387$ nm (ASAHI, 2012; WIELAND, 2016). However, UV can generate undesired side reactions, with a negative impact on the selectivity of the reaction. On the other hand, when applying visible light these side reactions can be minimized. Moreover, the cost associated with the use of visible light is much lower than that of UV lamps, especially when large scale applications are considered. Therefore, visible light is an attractive alternative to overcome the aforementioned issues (ANGNES *et al.*, 2015; WIELAND, 2016). However, a disadvantage of using sunlight to drive chemical transformations can be highlighted: the inability of organic molecules to absorb light in the visible range of the spectrum. Nevertheless, in order to absorb the visible light, a photocatalyst with color can be applied.

With the advances in photochemistry, several research topics have been developed. Among these, the most frequent topic related to visible light-driven chemical transformation is photoredox catalysis (WIELAND, 2016).

2.2.1 Photoredox Catalysis

The photoredox catalysis exploits the intensification of the redox activity in a photo-excited catalyst, which becomes a strong oxidant or a strong reductant. Considering that this activation mode occurs in moderate reaction conditions, *e.g.*, with non-hazardous reagents and using visible light, it proves to be an interesting and promising application in pharmaceutical synthesis (ZELLER, 2016; NOËL, 2017).

As previously stated, one issue of using visible light is that organic molecules do not absorb in the visible region. Thus, in order to utilize this energy provided by the visible light, organic or transition-metal based photocatalysts with color can be applied. Those are able to harvest visible light, reaching their excited states and mediating the single-electron transfer (SET) processes from the excited state (NICHOLLS; LEONORI; BISSEMBER, 2016). According to Ghosh (2016), the process can follow two paths (Figure 2):

1. reductive quenching cycle: the excited photocatalyst receive an electron from a donor and then returns to the ground state in reduced form.
2. oxidative quenching cycle: the excited photocatalyst donate an electron to an acceptor and then returns to the ground state in oxidized form.

Figure 2 - Quenching cycles of a photocatalyst.

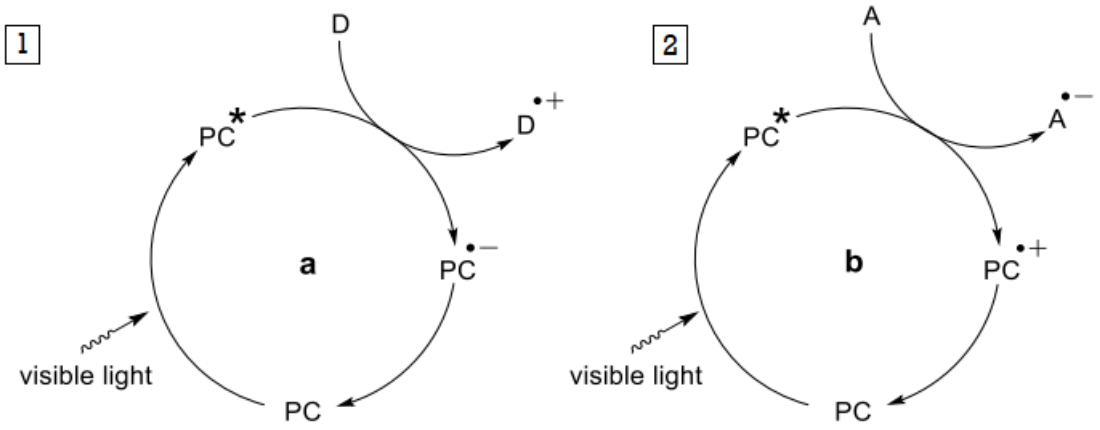

1- Reductive quenching cycle. 2 – Oxidative quenching cycle.
Reference: Ghosh (2016).

The interaction among these electronically photo-excited catalysts and an organic molecule is able to generate reactive intermediates that can result in synthetically useful bond constructions (SKUBI; BLUM; YOON, 2016).

Several studies have been carried out using photoredox catalysis for the synthesis of compounds, and organometallic polypyridyl transition metal complexes and organic dyes can be considered the most applied and efficient photocatalysts in organic synthesis (KÇNIG *et al.*, 2013; NARAYANAM; TUCKER; STEPHENSON, 2009; RAVELLI; FAGNONI; ALBINI, 2013; SCHULTZ; YOON, 2014; SHI; XIA, 2012; XUAN; XIAO, 2012). However, due the high cost and toxicity of transition-metal complexes, organic photosensitizers (metal-free) became an attractive option, since they commonly have low cost, long excited-state lifetime and high extinction coefficient (PITRE; MCTIERNAN; SCAIANO, 2016). The most common organic photosensitizers applied are methylene blue (CAMBIÉ *et al.*, 2017a; KALAITZAKIS *et al.*, 2015) and eosin Y (HARI; KO, 2014; MENG *et al.*, 2013).

These photochemical reactions can be carried out in microstructured reactors. Which has been the theme of several works due to the advantages of these systems, such as homogeneity in the spatial illumination and improvement in light penetration when compared to the large-scale reactors (MATSUSHITA *et al.*, 2007).

2.2.2 Photochemistry in microreactors

The microflow chemistry technology has attracted more attention along the years and became an independent field of research. An advantage of microflow reactors over conventional batch equipment is the superior light penetration in the system. Photochemistry in batch reactors is limited by to the Lambert-Beer law, which states that the light intensity decreases logarithmically along a path due to photon absorption. This limitation is not relevant in microflow systems since the narrow channels impose very low resistance to photon transport (MEYER *et al.*, 2007; WIELAND, 2016).

Moreover, another benefit of carrying out chemical reactions in small volumes is the easier control of reaction parameters, *e.g.*, pressure, temperature, residence

time and flow rate, resulting in an improvement of the conversion and enhanced energy efficiency (MEYER *et al.*, 2007; OELGEMÖLLER, 2012). Photochemical reactions in flow can occur in short time intervals when compared to batch reactors, minimizing by-product formation and increasing the productivity of the process (CAMBIÉ *et al.*, 2016).

Given the well-established advantages of microflow systems over batch reactors, several studies have been conducted to evaluate the performance of these devices in photochemical processes (AIDA *et al.*, 2012; AKWI; WATTS, 2018; YOSHIDA; KIM; NAGAKI, 2011). Although commercial microreactors have been widely adopted in photochemistry, several devices built *in-house* can also be found in the literature, allowing to adjust the characteristics of the microreactor according to the end application (COYLE; OELGEMÖLLER, 2008). Noël (2017) established that the correct selection of the reactor material is of paramount importance, since the majority of the capillaries used in microflow chemistry are made of perfluoroalkoxyalkane (PFA) and perfluoroethylenepropylene (FEP), and these materials tend to present a fast degradation, especially at higher energy wavelengths. Thus, studies have suggested the design of photomicroreactors based on alternative materials, such as quartz, glass, silicon, metal, and ceramic, accordingly to the type of reaction that will be carried out (COYLE; OELGEMÖLLER, 2008).

Another point for improvement is the energy efficiency of the photomicroreactors (NOËL, 2017). Thus, inspired by the Luminescent Solar Concentrator (LSC) technology, Cambié *et al*. (2017) developed a luminescent solar concentrator-based photomicroreactor (LSC-PM) to promote chemical reaction activated by sunlight. This photomicroreactor is composed by a synergistic integration of LSC and microflow chemistry, which allows an enhancement in the energy efficiency since it harvests the sunlight and waveguides this energy to the microchannels to promote the photochemical reactions (CAMBIÉ *et al.*, 2017a,c; ZHAO *et al.*, 2018b). The LSC-PM will be the theme of this work and, in order to contextualize it, the item 2.3 will give a general approach of the system, and further details will be explored in the next topics.

2.3 LUMINESCENT SOLAR CONCENTRATOR-BASED PHOTOMICROREACTOR (LSC-PM)

The LSC-PM was first presented in 2017 by Cambié *et al.,* with the objective of enabling chemical reactions driven by sunlight. As previously stated, the device merges microflow chemistry and the LSC principle, *i.e.*, the flow reactor was embedded in an LSC light guide, a dye-doped base of polydimethylsiloxane (PDMS), in which the luminescent particles were selected in a way that its emission profile matched the absorption spectrum of the photosensitizer. The dye-doped base of PDMS down-converts the energy to a narrow wavelength region and transports this energy towards the embedded microchannels, where the flowing reactants are transformed (CAMBIÉ *et al.*, 2017a).

To evaluate the performance of the LSC-PM a benchmark reaction was used in the system, the [4+2] cycloaddition of 9,10-diphenylanthracene (DPA) with singlet oxygen that was generated via photosensitization in the presence of methylene blue (MB) (ZHAO *et al.*, 2018a). In order to highlight the components of the LSC-PM, this work was segregated into two categories: light guide and flow. An illustration of the system's structure can be observed in the scheme presented in Figure 3.

Moreover, the device was built in a way that it could work either with diffuse or direct light. A control system was developed in order to enable constant conversion independent of the sunlight fluctuations during the day. The device and its characteristics will be elucidated in detail in the next topics.

2.3.1 LSC principle

The LSC system was proposed more than thirty years ago by Goetzberger and Greubel (1977). The project aimed an inexpensive and efficient energy generation system, where one of the main characteristics was the operation with direct and diffuse solar radiation, as a consequence of its high acceptance angle for incident light (GOETZBERGER; GREUBEL, 1978, 1977; WIELAND, 2016).

Figure 3 - Schematic representation of the LSC-PM system.

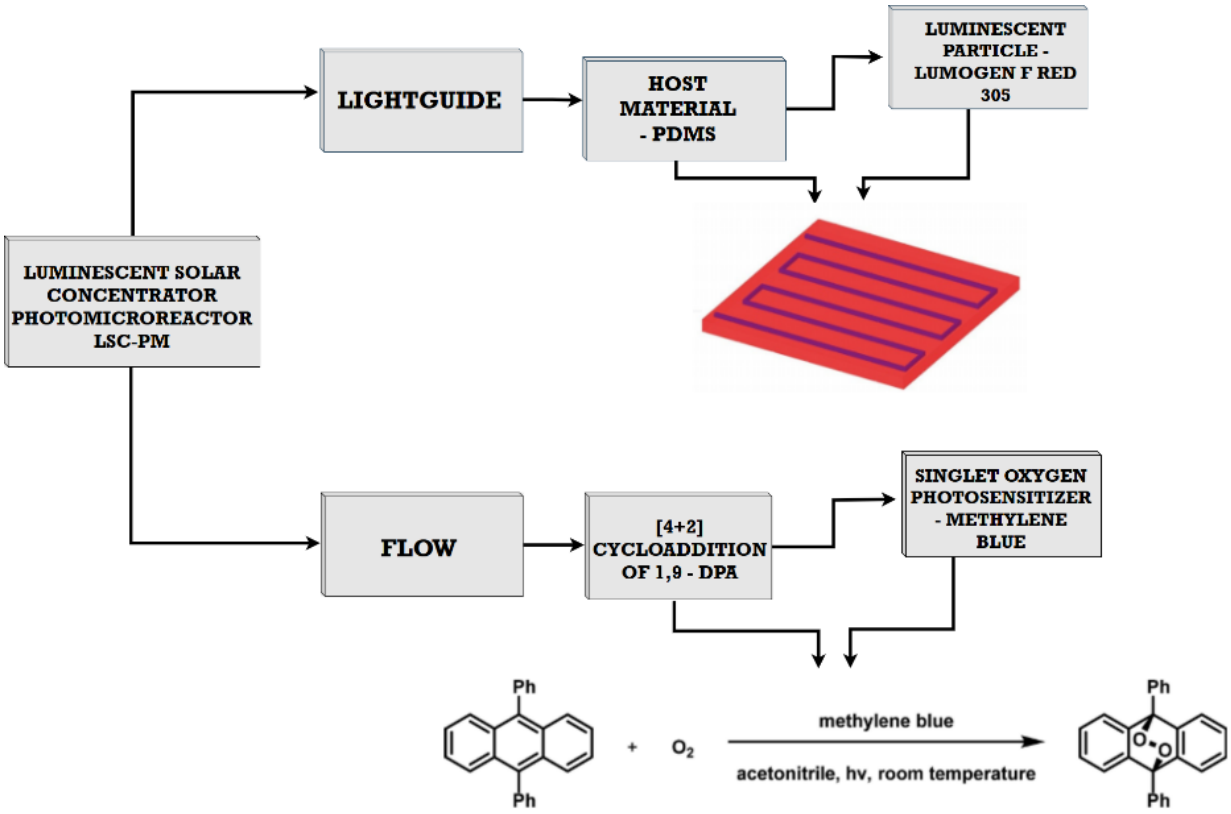

Reference: adapted from Cambié *et al*. (2017) and Zhao *et al.* (2018).

The operation of the system is quite simple, consisting of a light trapping and guiding concept. The system collector consists on a flat sheet of glass or polymer (more common), such as PDMS (CHOU; HSU; CHEN, 2015; YANG *et al.*, 2013) and polymethylmethacrylate (PMMA)) (LIU *et al.*, 2014; MEINARDI *et al.*, 2014), with a refractive index *n*, doped with fluorophores. The fluorophores function is the absorption and reemission of the absorbed light in high quantum efficiency (SARK *et al.*, 2008). Quantum dots, rare earths, and organic dots can be cited as the frequently employed fluorophores.

The quantum yield of the fluorophore will be responsible for the emission of the light in a longer wavelength or the dissipation of the absorbed light to heat. When emitted, the photon experiences a wavelength shift and, since the emission reaches the outside of the escape cone, the light is trapped through total internal reflection (TIR) in the LSC matrix (TUMMELTSHAMMER, 2016). Thus, the trapped radiation is wave-

guided and reaches the edges of the concentrator, where it can be converted into electricity by photovoltaic cells (Figure 4).

Figure 4 - Representation of the LSC system.

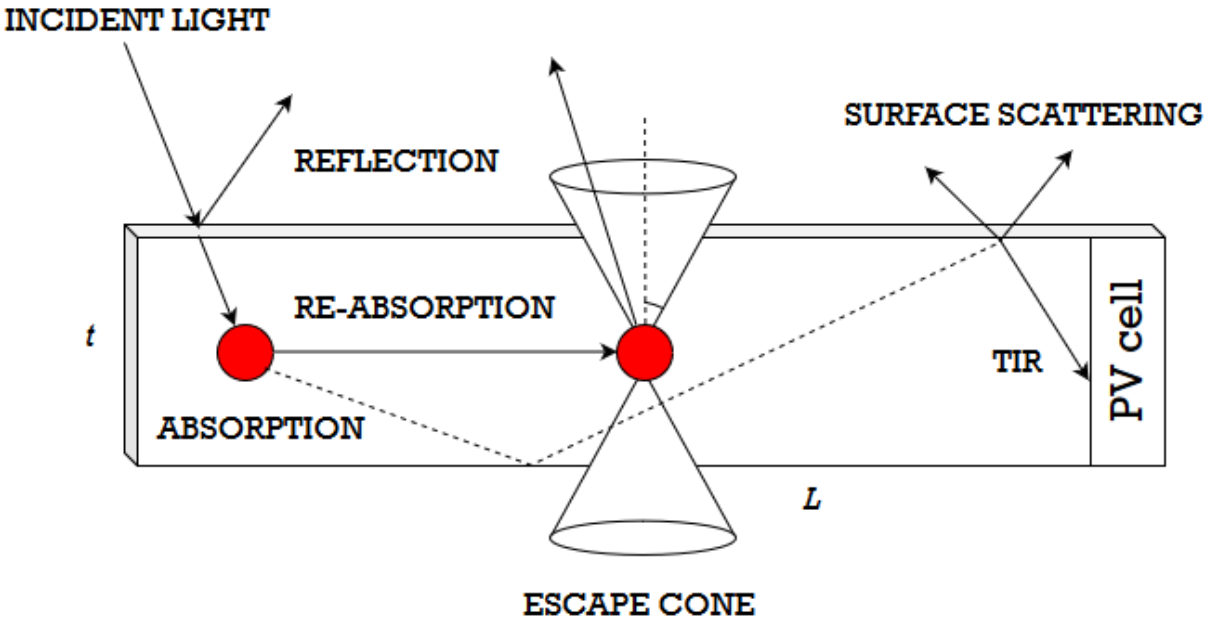

Reference: adapted from Richards (2006).

However, the LSC presents energy losses in the system. As Figure 4 demonstrates, reflection, re-absorption, and scattering can be considered some of the "photon fates" in the system, characterizing energy losses, since the ideal condition would be the TIR to the PV cell. This theme will be discussed in detail in this work.

Therefore, giving the broad application of the LSCs, different approaches have been reported aiming to improve their performance, such as the minimization of luminophore self-absorption losses (ERICKSON *et al.*, 2014; KRUMER *et al.*, 2013, 2017; SUMNER *et al.*, 2017; WU *et al.*, 2010), enhancement of power conversion efficiency (CORRADO *et al.*, 2013; DAS; NARAYAN, 2013; DESMET *et al.*, 2012; SARK *et al.*, 2008), and improvement of photon transport (ILAN; KELLEY, 2011; RONCALI; GARNIER, 1984).

2.3.2 Host material

The LSC-PM matrix is inspired in the LSC one. Therefore, a fundamental factor in an LSC is the selection of the light guide. Ideally, the host material must be inexpensive, highly transparent, with a broad refractive index (~1.5), photo-stable, and mechanically and chemically resistant. Thus, polymers have been frequently chosen as light guides since several materials in this class meet the required characteristics (EBRAHIMIPOUR; ASKARI; RAMEZANI, 2016).

Among the several options available, PMDS and PMMA are the most common choice. Despite the several studies involving PMMA (CORRADO *et al.*, 2013; KERROUCHE *et al.*, 2014; KRUMER *et al.*, 2013; LIU *et al.*, 2014; VAN SARK, 2013), Chou, Hsu and Chen (2015) alleged that this rigid substrate can restrict the applicability of the technology, and involves complicated fabrication techniques. Thus, PDMS became an interesting alternative for the construction of LSC devices, being studied in several works (APAKONSTANTINOU, 2016; CHOU; CHUANG; CHEN, 2013; MEINARDI *et al.*, 2014).

In fact, PDMS is the favorite host material for microscale fluid devices. This fact can be explained by its advantages, such as the low production cost compared to substrate materials such as silicon or glass, which allow fast prototyping; optical transparency (above wavelengths ~230 nm) and flexibility (BHAGAT; JOTHIMUTHU; PAPAUTSKY, 2007). Moreover, PDMS can be easily doped with Lumogen F Red 305 (reference dye) (HOFMANN *et al.*, 2006). Besides the criteria already cited, the refractive index, n, is also an important parameter for the design and optimization of these devices. The refractive index is, briefly, the ratio of the velocity of light of a certain wavelength in the vacuum relative to the velocity of light passing through a specific material (BRYDSON, 2017). The refractive index interferes directly in the proportion of the trapping-guiding process of the photons inside the device and, according to Mouedden (2016), the higher the refractive index, the larger will be the number of trapped photons. PDMS presents a moderate refractive index of 1.41 (CAMBIÉ *et al.*, 2017a).

2.3.3 Luminescent particles

The doping of the material is pivotal to the system since the luminescent particles are responsible for the absorption and reemission of the radiation in a longer wavelength. As already stated in item 2.3.1, the commonly utilized luminescent particles in LSC are organic dyes, quantum dots, and rare earths materials. Among these materials, organic dyes have been the most commonly used, due to their low cost, easy production, and abundance.

Among the species of organic dyes, since the 1970s and 1980s, the most used ones for this purpose are coumarins, rhodamines, and perylenes derivatives (MANZANO CHÁVEZ, 2017). The Lumogen F Red 305 (Red 305), from the perylene group, has been broadly applied in LSC systems (DESMET *et al.*, 2012; DIENEL *et al.*, 2010; KRUMER *et al.*, 2017; SLOOFF *et al.*, 2008) due its good solubility, high quantum yields and broad Stokes shift (BALABAN, 2013). Furthermore, this compound presents higher photostability than the others Lumogen F group dyes (BASF, 1997).

2.3.3.1 Light transport and loss factor

In the LSC-PM the ideal condition for light transport is the TIR, where the luminescent particle absorbs the light and re-emit it in a way that a TIR in the system guides it to the reaction centers. However, as already stated, the LSC system and consequently, the LSC-PM, still presents limited efficiencies due to energy losses in the system. These losses can be classified from the observation of the possible photon fates, and those photon fates can be seen in Figure 5.

Figure 5 - Representation of possible fates of the photons in the moment that the light strikes the LSC-PM device.

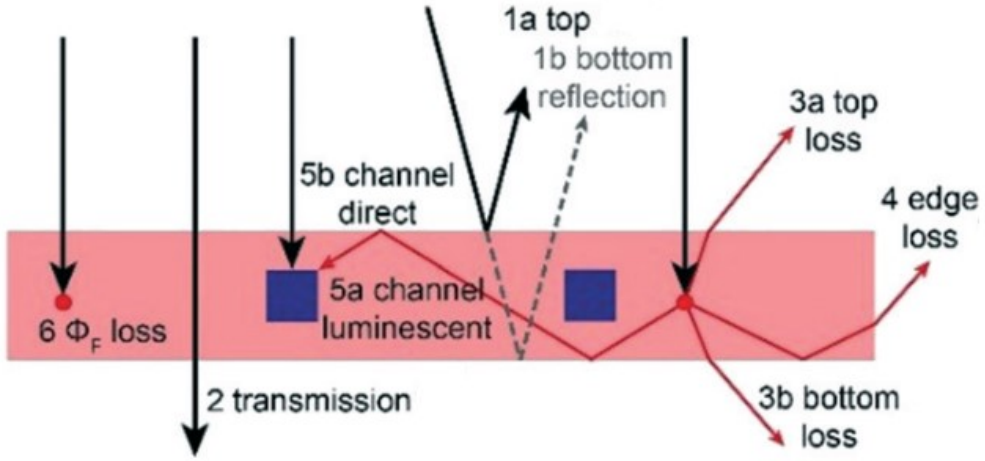

Reference: Cambié *et al*. (2017).

As shown in Figure 5 the photon fates in the system can be classified as:

- reflection (1) and transmission (2): According to Chavéz (2017), when light impinges on a flat surface it passes through a medium with a refractive index n_1 to a medium with a different refractive index, n_2. This can result in two fates: reflection and transmission through the material. These characteristics determine a Fresnel loss type material, where part of the light is reflected and part of the light is transmitted.

- emission (3): this loss can be induced by the incidence of light in the scape cone, where it can cause a top or bottom emission.

- edge emission (4): in the LSC-PM system, the edge emission is not desired and, consequently, it is considered a loss.

- reaction media absorption (5): occurs when light is absorbed by the media and not re-emitted to the system.

- non-radiative losses (6): a non-radiative dissipation of the energy previously absorbed by the luminescent particles.

In order to optimize the performance of the light-dependent systems and quantify these losses, ray-tracing simulations are of paramount importance. This can be considered a result of the ability of these algorithms to elucidate the photon behavior in the analyzed domain.

2.3.3.1.1 Ray-tracing simulations

Currently, ray-tracing simulation is an approach broadly applied in several areas such as radio (ATHANAILEAS *et al.*, 2010; CHEN; DELIS; BERTONI, 2004), acoustics (JANG; HOPKINS, 2018; MO *et al.*, 2016), gravitational waves (DING; WAN; YUAN, 2003; JONES; BEDARD, 2018; VADAS; FRITTS, 2009) and optics (HU *et al.*, 2015; KERROUCHE *et al.*, 2014; REHMAN, 2019).

Trough optical ray-tracing simulation, it is possible to simulate the path of the rays by combing the principles of traditional geometric optics and the Monte Carlo method. Dissipation of light is determined by the optical properties of surfaces, materials and emission sources (KERROUCHE *et al.*, 2014). Since these simulations work through the stochastic Monte-Carlo probability method, random numbers are considered to determine the direction, position, and energy, among other parameters (JI; ZHANG, 2019). The fate of the rays can be elucidated since these algorithms are able to evaluate the rays that are absorbed, reflected, refracted, diffracted and scattered in the domain.

Thus, the application of ray-trace modeling can be considered, nowadays, indispensable for the design, performance evaluation and optimization of optical systems. In this context, several studies have been devoted to applying ray-trace modeling in those systems. Chávez (2017), simulated three LSC models, the first one made of a PMMA matrix and doped with a red dye. The second and third LSC models were doped with thulium: one of them was a glass doped with thulium particles, while the other one consisted of a pure glass coated with thulium. The main objective was to

find the characteristics that affect the optical efficiency of the system and optimize these parameters. The simulations were carried out using the optical engineering software LightTools®. The optical losses in the red dye model were elucidated and quantified and then compared with experimental data, showing a good agreement and enabling the validation of the model. On the thulium models, the author concludes from the results of the simulation that the LSC performance might be improved by adding thin film layers in the glass, such as anti-reflection coating and selective filters to allow visible light and reflect near-infrared photons into the glass.

Haines *et al*. (2012), evaluate the effect of the perylene diimide in PMMA films cast onto glass substrates. The Monte Carlo ray-trace algorithm was developed using MATLAB® software. The ray-tracing results were compared with the experimental ones and showed a good agreement. From the data obtained the authors concluded that the major factor that affects the performance of the LSC is the luminescence quantum yield of the dye. Moreover, with the simulation data coupled with the experimental output, the authors concluded that the perylene diimide is not an optimized material for LSC applications.

Kumar, Velu, and Balasubramanian (2019) proposed a novel free form lens design for collimating UV light from an LED, where four models were proposed: three surfaces of free form and one with total internal reflection. A ray-tracing simulation with the ZEMAX OpticsStudio® 15.5 ray-tracing software was employed to observe the performance of the lens. The authors concluded from the ray-tracing simulations that the designed lens presented a better collimation angle of ±2° with improved efficiency of 58.88% when compared to 34% of the existing lens.

Vishwanathan *et al*. (2015) compared the performance of the flat and bent LSC-photovoltaic (LSC-PV) doped with Lumogen Red 305 dye, via Monte Carlo ray-tracing simulations on LightTools® software. The authors modeled two types of light sources in order to simulate the direct and diffuse irradiance, the first one was a perpendicularly directed light source and the second one a Lambertian source. The sun sources were modeled with the AM 1.5G spectrum. The best optical efficiencies were found for the flat LSC-PV, an observation indicated as a consequence of the higher loss of the rays in the bent LSC, due to its bent light guide. The concentration

of the dye was varied in the simulations as well. From the simulations, the authors observed that the low concentration of dye resulted in insufficient absorption of the light. However, higher concentration leads to losses by reabsorption, decreasing its optical efficiency. The efficiency of the system with very low concentrations of the dye was about 10% and increasing the dye concentration resulted in a maximum efficiency of 20%. This maximum efficiency can be explained by the excessive reabsorption and eventually generation of non-emissive dye clusters in the light guide.

Cambié *et al.* (2017) simulated the LSC-PM photon path with a modified version of PvTrace, a Python-based Monte-Carlo ray-tracing algorithm for LSC simulations, in order to guide further design and optimization of the device. Good agreement was found between the experimental and simulated data. Based on the simulations, the authors were able to optimize the system from an exchange in the dimensions of the channels.

Therefore, it is evident from the studies reported above that there is a clear need to elucidate the losses in the optical systems in order to evaluate their performance and optimize them. This scenario motivated the studies carried out in this work.

2.3.4 Flow characterization

The oxygen singlet photo-oxidation of 9,10 diphenylanthracene (DPA) to its corresponding endoperoxide has been extensively studied since it is a light-dependent reaction, allowing simple quantification of the reaction advance (PITRE *et al.*, 2015).

The molecular oxygen became an interesting “green reagent” due to its negligible environmental impact. Moreover, other advantages are its low cost and large availability (SEEBERGER, 2011). There are many ways to generate oxygen singlet, including the photosensitized generation. It can be explained due to the fact that the photosensitized generation is a simple and controllable method, requiring only light in an appropriate wavelength, oxygen, and a photosensitizer able to absorb this energy and excite the oxygen to its singlet state (DEROSA; CRUTCHLEY, 2002). The

sensitizing potential of rose bengal, methylene blue, and hematoporphyrins can be highlighted (KRUK, 1998).

This oxidation can occur in several ways, where the ene, [2+2] and [4+2] cycloadditions can be highlighted as powerful methods for the addition of molecular oxygen (CLENNAN; PACE, 2005). The [4+2] mechanism for the reversible binding of $^1O_2$ in aromatic compounds is widely exploited for the production of chemical traps, having in mind that the endoperoxide formed can be considered a specific product for the reaction with $^1O_2$. The detection of these endoperoxides formed in the reaction can be provided through a HPLC–MS analysis (MARTINEZ *et al.*, 2006).

Therefore, for the LSC-PM system, a [4+2] cycloaddition of singlet oxygen generated via methylene blue photosensitization to 9,10 diphenylanthracene was used as a benchmark reaction since a light-dependent reaction can be monitored through UV-Vis spectrophotometry (Figure 6). Acetonitrile can be used as a solvent due to its non-absorbing property (CAMBIÉ *et al.*, 2017a).

Figure 6 - 9,10 diphenylanthracene conversion to its respective endoperoxide.

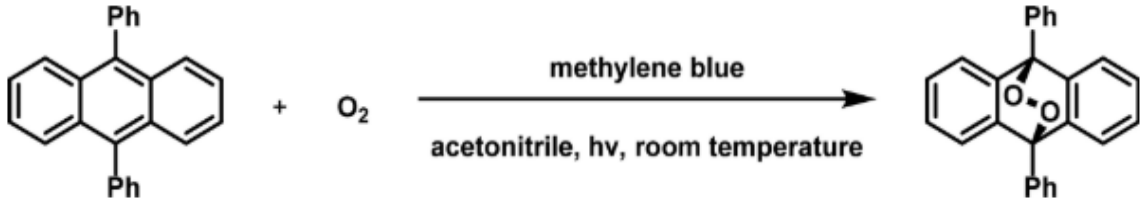

Reference: Cambié *et al*. (2017).

Despite the several advantages of the use of sunlight already stated, the necessity of constant irradiation for the chemical synthesis represents a challenge, due to the constant fluctuations of photon flux during the day, *i.e.*, weather changes are of great impact on the reaction efficiency. Thus, a control system to mitigate the impact of the fluctuation is crucial.

2.3.4.1 Control system

The constant evolution of methods for chemical synthesis has been closely accompanied by a higher degree of automation of the equipment involved. In this context, low-cost digital control can be successfully applied to the improvement of the performance of chemical reactors applied to the synthesis of added-value compounds (FITZPATRICK; BATTILOCCHIO; LEY, 2016).

Photochemical synthesis based on sunlight is one of the fields that clearly presents a need for control systems. The changes in the irradiation during the day has a huge impact on the efficiency of the reaction. Although intensive research has been conducted for the automatization of these systems, on-line analytical techniques still represent the strategy most applied (FABRY; SUGIONO; RUEPING, 2014). However, this approach is not indicated for processes driven by sunlight, once the light irradiation can change drastically and high time delays in the measurements would generate undesirable conversion fluctuations (ZHAO *et al.*, 2018).

Based on this scenario, Zhao *et al*. (2018), proposed a real-time reaction control system for the LSC-PM, in order to maintain a constant conversion despite the irradiation fluctuations during the day. This control system works through the adjustment of the reactor's residence time based on the light intensity in a specific time of the day.

Figure 7 - Representation of the LSC-PM real-time reaction control system.

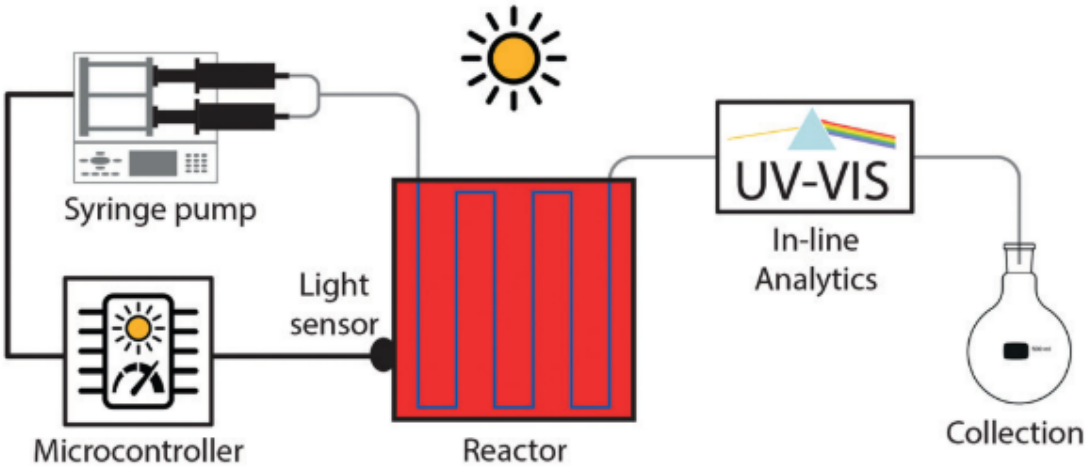

Reference: Zhao *et al.* (2018).

Figure 7 shows a representation of the items that constitute the real-time reaction control system. A light sensor is placed at the edge of the microreactor and is responsible for monitoring the photon flux in the device. Since the light intensity at the LSC-PM's edge is proportional to the photon flux reaching the microchannels, this measurement can be used to characterize the optical performance of the device. This light sensor is connected to a microcontroller that automatically adjusts the pump power depending on the light intensity read. The time delay involved in reading the voltage, executing the control algorithm and sending the corresponding action to the pump is c.a. 500 ms. As previously indicated, the reaction of [4+2] cycloaddition of singlet oxygen to 9,10 diphenylanthracene can be continuously analyzed via UV-VIS spectrometer, since the reaction kinetics is light-limited (ZHAO *et al.*, 2018).

Thus, it is possible to declare that the light distribution is not the only parameter to be considered when analyzing and optimizing the LSC-PM applied to the synthesis of added-value compounds: the microflow also has a huge effect on the reactor's performance. Characterizing the flow is pivotal for the optimization of the microreactor and computational fluid dynamics (CFD) algorithms can be successfully applied for this purpose (CHETVERUSHKIN *et al.*, 2004).

2.3.5 CFD applied to flow distribution characterization

CFD is a powerful tool that can be applied in several engineering fields. This tool can be employed to observe the physical events that occur in the flow of fluids on a determinate domain. These events can be often related to the phenomena associated with dissipation, diffusion, convection, boundary layers, and turbulence. CFD works with fluids in motion and analyzes how the behavior of the fluid can influence processes such as heat and mass transfer. It works through the use of algorithms and numerical methods to provide flow information that with traditional techniques would be considered difficult, expensive or inconceivable, *e.g.*, analytical solutions or experiments (TU; YEOH; LIU, 2018).

Thus, in this context, CFD has been shown to be useful for the analysis of the flow characteristics and reactor performance, being able to capture the presence of dead zones, the velocity and concentration fields, and evaluate the transport of radiation. In this sense, several studies have been carried out to investigate the flow behavior in photomicroreactor. Investigations on the design and optimization of microreactors with these tools have been highly successful for liquid phase systems. This can be attributed to the fact that the behavior of incompressible liquid along with the laminar flow regime, characteristic of micrometric scale, usually generate good results on CFD simulations (SANTANA; SILVA; TARANTO, 2019). Therefore, many studies have applied CFD tools to observe the significant influences of microfluidic geometries and flow on the performance of the operating system (COMMENGE *et al.*, 2002; GRIFFINI; ASTERIOS, 2007; O-CHAROEN; SRIVANNAVIT; GULARI, 2007; ODIBA *et al.*, 2016).

Chetverushkin *et al.* (2004) showed the possibility to integrate the reactor hydrodynamics, radiation intensity, and kinetics. The model was applied to several types of reactors. The authors conclude that the difference in the performance of the can be due to the light intensity distribution in the reactors, which changed when the lamp was repositioned. Moreover, the authors conclude that the UV transmittance of the fluid and the fluid flow rate also interferes on the reactor performance.

Based on that, it is evident the range of possible uses of CFD for accurate modeling of fluid flow in photochemical reactors, which motivated part of the studies performed in this work.

3 MATERIALS AND METHODS

3.1 CFD SIMULATION

The CFD modeling was based on the indoor kinetic investigation carried out by Zhao *et al.* (2018). The steps of the investigation can be seen in Figure 8. The syringe pump is responsible to insert the solutions with DPA and MB (0.2 mM and 0.4 mM in acetonitrile respectively to the microreactor). The white led strip presented in Figure 8 is placed onto a cylindrical box, and a power supply is responsible to power this led strip. In the outlet of the microreactor the reaction mixture is analyzed by a UV-VIS spectrometer, where the absorbance is further utilized to calculate the conversion of the reaction. In order to observe the behavior of the system in different light intensities the LED strip intensity was varied. The kinetic curves were obtained through a flow rate change under each light intensity, and the correspondent voltage value under each light intensity detected by the microcontroller was recorded as well (Zhao *et al*. 2018). The data utilized in this work was provided by the Noël Research Group and can be seen in Appendix A, Table A1.

Figure 8 – Flow scheme of the indoor kinetic experimental procedure.

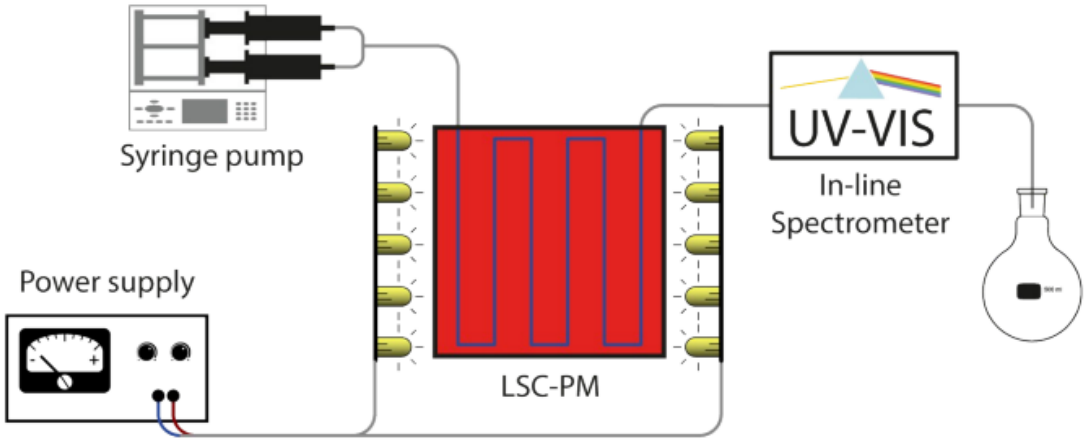

Reference: Zhao *et al.* (2018).

3.1.1 Geometry

The geometry was built in three dimensions to simulate laminar and single-phase flow, as well as the transport of chemical species. All the sections of the experimental device were taken into account to enable an optical analysis, which will be described in a further section. Figure 9 shows the microreactor geometry assembled in COMSOL Multiphysics® (version 5.3a) software and the dimensions of it. The model was built based on the device proposed by Cambié *et al.* (2018), and it consists of an inlet (A), a reaction channel (B), and a mold border (C).

Figure 9 – (1) Representation of the LSC-PM built in COMSOL Multiphysics® (version 5.3a) software. (2) Dimensions of the LSC-PM device.

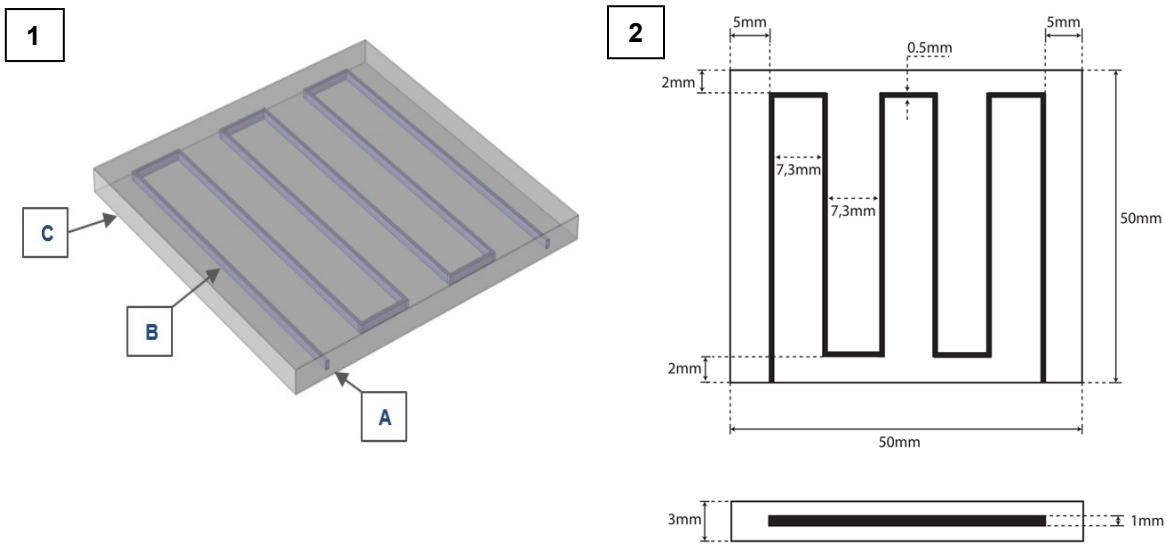

Reference: author (2019).

3.1.2 Grid independence test

In order to evaluate the degree of numerical uncertainty due to the construction of the mesh, the method proposed by Celik *et al.* (2008), the so-called Grid Convergence Index (GCI), was applied. The conversion of DPA at the outlet of the photomicroreactor was used for the implementation of the method. To calculate the

refinement errors an algorithm was developed in the free software GNU Octave 4.2.1, based on the routine of Celik *et al.* (2008) (Appendix A).

Three meshes were created. The coarsest mesh had 1,790 elements, the intermediate had 43,290 elements, while the finest mesh had 766,544 elements. These three meshes were made with a refinement ratio greater than 1.3 (CELIK *et al.*, 2008).

The estimated numerical uncertainty of the refined mesh (GCI21) and the intermediate mesh (GCI32) were 0.23% and 0.46%, respectively. Since the results were close to zero, it is possible to conclude that the meshes are very related, making possible to carry out the simulation procedure with the intermediate mesh.

3.1.3 Mathematical model

The mathematical model consisted of a system of nonlinear partial differential equations describing multidimensional, time-dependent and single-phase flow problem. The overall mass conservation was calculated according to Eq. (2) (BIRD; STEWART; LIGHTFOOT, 2007).

$$\frac{\partial v_x}{\partial x} + \frac{\partial v_y}{\partial y} + \frac{\partial v_z}{\partial z} = 0 \tag{2}$$

where v_x, v_y and v_z are *x*, *y,* and *z*-velocity components, respectively, obtained from the Navier-Stokes equations (Eq. (3) to (5)) (BIRD; STEWART; LIGHTFOOT, 2007).

$$\rho\left(\frac{\partial v_x}{\partial t} + v_x\frac{\partial v_x}{\partial x} + v_y\frac{\partial v_x}{\partial y} + v_z\frac{\partial v_x}{\partial z}\right) = -\frac{\partial P}{\partial x} - \left[\frac{\partial \tau_{xx}}{\partial x} + \frac{\partial \tau_{yx}}{\partial y} + \frac{\partial \tau_{zx}}{\partial z}\right] \tag{3}$$

$$\rho\left(\frac{\partial v_y}{\partial t} + v_x\frac{\partial v_y}{\partial x} + v_y\frac{\partial v_y}{\partial y} + v_z\frac{\partial v_y}{\partial z}\right) = -\frac{\partial P}{\partial y} - \left[\frac{\partial \tau_{xy}}{\partial x} + \frac{\partial \tau_{yy}}{\partial y} + \frac{\partial \tau_{zy}}{\partial z}\right] \tag{4}$$

$$\rho\left(\frac{\partial v_z}{\partial t} + v_x\frac{\partial v_z}{\partial x} + v_y\frac{\partial v_z}{\partial y} + v_z\frac{\partial v_z}{\partial z}\right) = -\frac{\partial P}{\partial z} - \left[\frac{\partial \tau_{xz}}{\partial x} + \frac{\partial \tau_{yz}}{\partial y} + \frac{\partial \tau_{zz}}{\partial z}\right] \tag{5}$$

where P is the pressure and τ_{ij} are the components of the stress tensor given by Newton's law of viscosity, according to Eq. (6) to (11) (BIRD; STEWART; LIGHTFOOT, 2007).

$$\tau_{xx} = -\mu\left[2\frac{\partial v_x}{\partial x}\right] + \frac{2}{3}\mu\left(\frac{\partial v_x}{\partial x} + \frac{\partial v_y}{\partial y} + \frac{\partial v_z}{\partial z}\right) \tag{6}$$

$$\tau_{yy} = -\mu\left[2\frac{\partial v_y}{\partial y}\right] + \frac{2}{3}\mu\left(\frac{\partial v_x}{\partial x} + \frac{\partial v_y}{\partial y} + \frac{\partial v_z}{\partial z}\right) \tag{7}$$

$$\tau_{zz} = -\mu\left[2\frac{\partial v_z}{\partial z}\right] + \frac{2}{3}\mu\left(\frac{\partial v_x}{\partial x} + \frac{\partial v_y}{\partial y} + \frac{\partial v_z}{\partial z}\right) \tag{8}$$

$$\tau_{xy} = \tau_{yx} = -\mu\left[\frac{\partial v_y}{\partial x} + \frac{\partial v_x}{\partial y}\right] \tag{9}$$

$$\tau_{yz} = \tau_{zy} = -\mu\left[\frac{\partial v_z}{\partial y} + \frac{\partial v_y}{\partial z}\right] \tag{10}$$

$$\tau_{zx} = \tau_{xz} = -\mu\left[\frac{\partial v_x}{\partial z} + \frac{\partial v_z}{\partial x}\right] \tag{11}$$

where μ is the mixture dynamic viscosity which was calculated by Eq. (12) (GRUNBERG, L.; NISSAN, 1949).

$$\ln \mu = \sum_i x_i \ln \mu_i \tag{12}$$

μ_i is the dynamic viscosity for each species in the mixture and x_i is the mole fraction of the component i in the liquid mixture. As initial condition, null velocity was adopted, *i.e.*, before the start of the calculation, the velocity was equal to zero in the entire computational domain (Eq. (13)). At the inlet of the reactor, a given average value was

imposed for the velocity in the *x*-direction (Eq. (14)), while at the outlet null gauge pressure was prescribed (Eq. (15)). In addition, the no-slip condition was defined for all the walls (Eq. (16)) (tangential and normal velocity components equal to zero, representing impermeable and rigid walls).

$$v(t=0)=0 \tag{13}$$

$$v_x(x=0,\forall y,\forall z,t>0)=\overline{v_{x,in}} \tag{14}$$

$$P(x=L,\forall y,\forall z,t>0)=0 \tag{15}$$

$$v_{\vec{n}}=v_{\vec{t}}=0 \tag{16}$$

The transport of the DPA, took as model species, was modeled using the equation of continuity for the chemical species, given by Eq. (17) (BIRD; STEWART; LIGHTFOOT, 2007).

$$\frac{\partial C_i}{\partial t}+\left(v_x\frac{\partial C_i}{\partial x}+v_y\frac{\partial C_i}{\partial y}+v_z\frac{\partial C_i}{\partial z}\right)=\left(\frac{\partial J_{i,x}}{\partial x}+\frac{\partial J_{i,y}}{\partial y}+\frac{\partial J_{i,z}}{\partial z}\right)-kC_i \tag{17}$$

where C_i is the concentration of the DPA, k is the rate constant for pseudo-first order reaction and $J_{i(x,y,z)}$ represent the diffusive flux of the species in the *x*, *y* and *z*-directions, given by Fick's law (Eq. (18) to (20)) (BIRD; STEWART; LIGHTFOOT, 2007).

$$J_{i,x}=-D_{i,m}\frac{\partial C_i}{\partial x} \tag{18}$$

$$J_{i,y}=-D_{i,m}\frac{\partial C_i}{\partial y} \tag{19}$$

$$J_{i,z} = -D_{i,m}\frac{\partial C_i}{\partial z} \tag{20}$$

where $D_{i,m}$ is the species diffusivity in the mixture, expressed by Eq. (21) (MCGEE, 1991).

$$D_{i,m} = \frac{1 - y_i}{\sum_{j,j\neq i}\left(\frac{y_j}{D_{ij}}\right)} \tag{21}$$

The binary molecular diffusion in liquids (D_{ij}) was calculated through Wilke-Chang correlation given by Eq. (22) (BIRD; STEWART; LIGHTFOOT, 2007).

$$D_{ij} = 7.4 \times 10^{-8} \times \frac{\sqrt{\phi_j M_{w,j}}T}{\mu_j V_i^{0.6}} \tag{22}$$

where ϕ_j is an association parameter for the solvent, T is the absolute temperature, $M_{w,j}$ is the molecular weight of the solvent, μ_j is the viscosity of the solution and V_i is the molar volume of the solute at normal boiling point. Table 1 presents the physical properties of the species.

Table 1- Physical properties of the species.

Species	**Formula**	M_i	μ_i^*	V_i^*	ϕ_j^*	D_{ij} **(cm²·s⁻¹)****	
		(g·mol⁻¹)	**(cP)**	**(cm³·mol⁻¹)**	**(-)**	MB	DPA
Acetonitrile	C_2H_3N	41.05	0.34	51.2	1	1.18×10^{-5}	1.63×10^{-5}
MB	$C_{16}H_{18}ClN_3S$	319.85	0.909	379.2	1	-	1.24×10^{-5}
DPA	$C_{26}H_{18}$	330.42		373.9	1	-	-

Reference: *WELTY *et al.*, (2008); **calculated by Eq. (22).

A known concentration of DPA was imposed at the inlet of the reactor (Eq.

(23)), while zero derivative of the concentration was prescribed at the outlet. In addition, the initial condition for the concentration of specie i was the same as in the feed stream (Eq. (24)).

$$C_i(x = 0, \forall y, \forall z, t > 0) = C_{i,in} \tag{23}$$

$$C_i(t = 0) = C_{i,0} = C_{i,in} \tag{24}$$

3.1.4 Computational procedure

The equations presented in section 3.1.3 were solved using COMSOL Multiphysics® software (Burlington, MA, version 5.3a) using the finite element method. The computer utilized in the simulations was an Intel® Core™ @3.60GHz, 32 GB CPU of RAM and 64-bit Windows operating system. An irreversible pseudo-first order kinetics was assumed for the benchmark reaction. The fitting of the kinetic model to the experimental data (conversion versus residence time) considering different powers measured at an edge of device is presented in Appendix A (Table A1). The pseudo-first order specific rate constant was then determined according to Eqs. (25) to (28) (LEVENSPIEL, 1999).

$$A \rightarrow B \tag{25}$$

$$-r_i = -\frac{dX_i}{dt} = k(1 - X_i) \tag{26}$$

$$\int_0^{X_i} \frac{dX_i}{1 - X_i} = k \int_0^t dt \tag{27}$$

$$-\ln(1 - X_i) = kt \tag{28}$$

Eq. (28) represents a straight line with a slope equal to k. The plot $-\ln(1-X_i)$ *versus* t were created for each power evaluated (see Appendix A, Figure A1). Since different values of the pseudo-first order rate constant was obtained for each tip power tested, an equation relating *k* and *P* was obtained by second-order polynomial regression (Eq. (29)), with $R^2 = 0.9997$.

$$k(P) = 0{,}2420 \times P - 0.0792 \times P^2 \qquad (29)$$

Figure 10 presents the adjust of the second-order polynomial described by Eq. (29) to the experimental data.

Figure 10 - Relation of the rate constant (k) and the power (P).

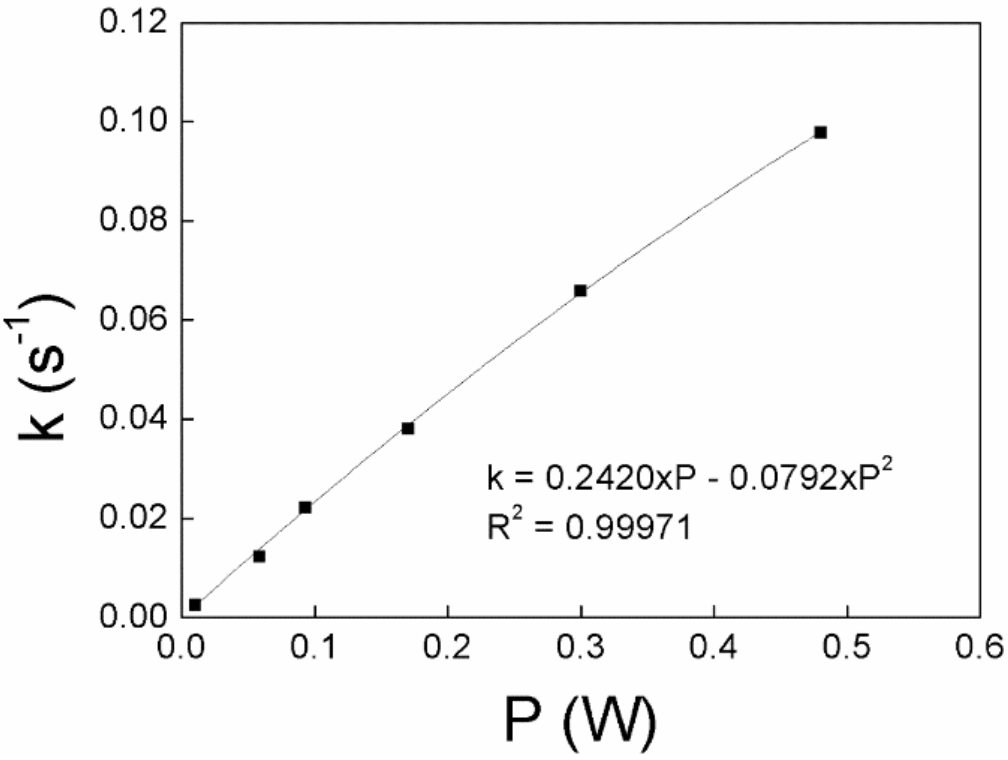

Reference: author (2019).

The DPA concentration was specified as $10^{-4}\ \mathrm{mol} \cdot \mathrm{L}^{-1}$ at the reactor's inlet. Moreover, the average inlet velocity was calculated by Eq. (30) for each power tested.

$$v_{ave,in} = \frac{V}{A \cdot \tau} \tag{30}$$

where *V* is the reactor's volume, *A* is the cross-section area of the microchannel and *τ* is the residence time.

Firstly, constant tip powers were considered to validate the computational model with the experimental data. Additionally, simulations were carried out varying the tip power through time according to predefined functions (rectangular, triangular and sinusoidal) (see Fig. 11). These power disturbances aimed to represent the variation of solar intensity during the day. It should be highlighted that the photon distribution within the LSC-PM was not solved in this part of the study and the tip power, proportional to the photon flux that the reaches the top of the device, was then taken as reference.

Figure 11 - Different forms for power disturbances as a function of time developed in the COMSOL Multiphysics® software: (a) rectangular, (b) triangular and (c) sinusoidal.

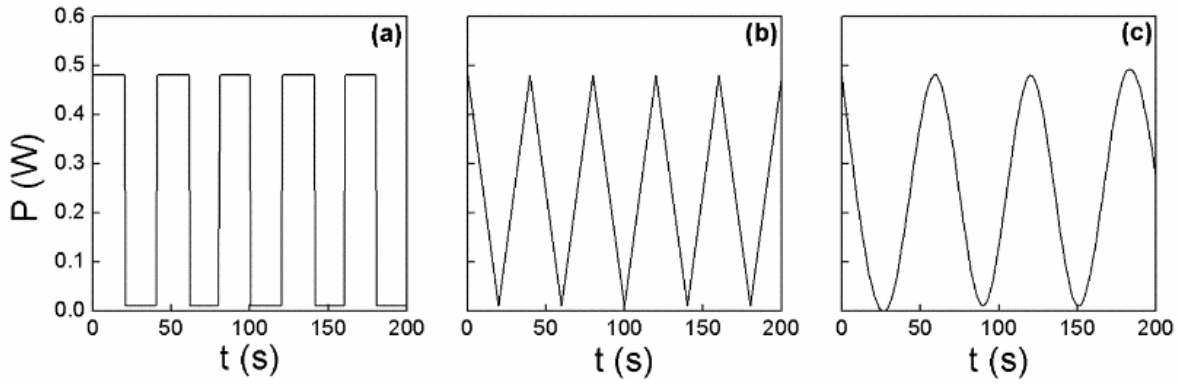

Reference: author (2019).

A feedforward control system was developed to maintain a stable DPA conversion due to power variations over time. Therefore, the mass balance was used to know how the velocity varies with the power (Eq. (18)). Considering steady-state and one-dimensional plug flow in the x-direction (Eq. (31)), the mass balance was reduced to Eq. (32).

$$v_x \frac{\partial C_i}{\partial x} \gg \frac{\partial J_i}{\partial x} \tag{31}$$

$$v_x \frac{dC_i}{dx} = -kC_i \tag{32}$$

In terms of conversion (LEVENSPIEL, 1999):

$$F_{i,0} \frac{dX}{dV} = kC_{i,0}(1 - X) \tag{33}$$

$$V = -\frac{F_{i,0}}{kC_{i,0}} \times ln(1 - X) \tag{34}$$

where V is the volume of reactor and $F_{i,0}$ is the molar feed rate of species i. Considering the definition of space time (τ) given by Eq. (35) (LEVENSPIEL, 1999), the velocity as a function of the tip power was specified according to Eq. (36).

$$\tau = \frac{C_{i,0}V}{F_{i,0}} = \frac{V}{\dot{Q}} = \frac{V}{vA} \tag{35}$$

$$v = -\frac{V}{A \ln(1 - X)} \times k(P) \tag{36}$$

Fig. 12 represents the block diagram created to represent the control system studied herein. First, the light is incident on the reactor, where the pseudo-first order volumetric reaction occurs. The power is read in the light detection circuit and a signal is sent to the controller. Finally, the controller adjusts the velocity at the reactor's inlet, according to Eq. (36). It can be highlighted that there is a delay when reading the power and sending the response in the form of the velocity variation at the reactor's inlet. This short delay was approximately 0.5 s (500 ms) in the reference experimental setup (ZHAO *et al.*, 2018), making it a real-time control system. This time delay was also considered in the simulations, firstly based on the experimental measurements and

then extrapolated to different scenarios to assess the performance of the control system in adverse conditions.

Figure 12 - Block diagram of the LSC-PM simulation.

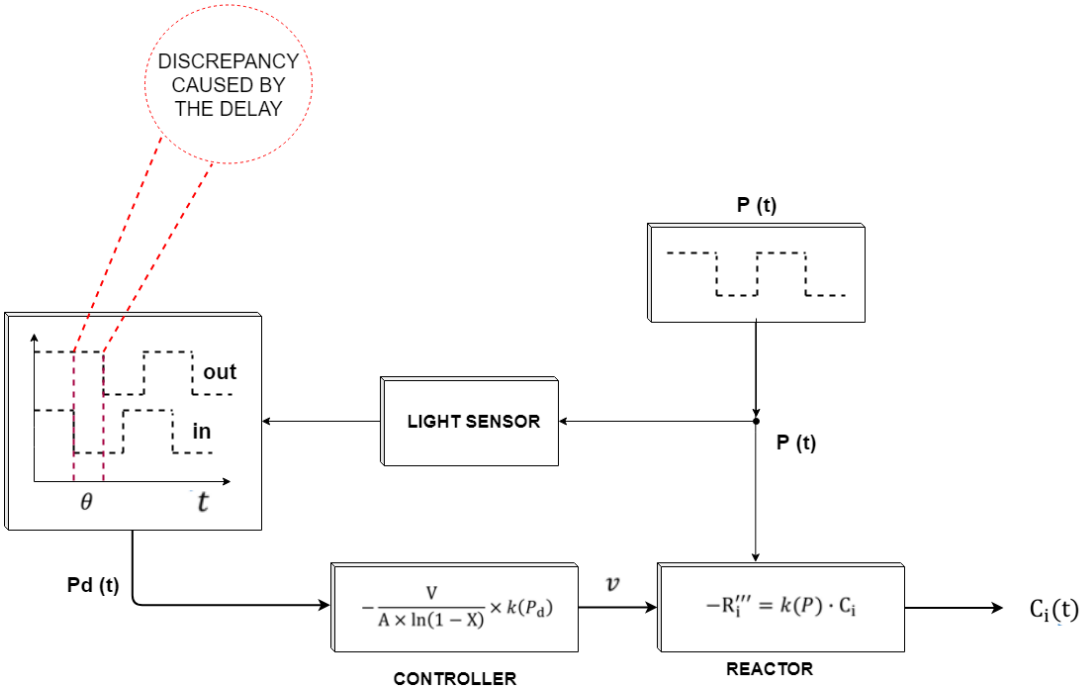

Reference: author (2019). *P(t): incident power in the LSC-PM.*Pd(t): power with a delay. *v: velocity variation in the reactor's inlet.

The time-dependent simulations were run for 200 s with variable time step-size determined by the BDF algorithm. The system of partial differential equations was solved segregated, *i.e.,* weakly coupled. First, a direct solution (using PARDISO solver) was obtained for the momentum conservation equations and then the species conservation equation was solved iteratively (using GMRES solver with geometric multigrid preconditioner), considering the velocity field previously calculated. The nonlinear equations were solved using Newton's method.

Furthermore, since flow non-idealities can occur in the reactor, causing undesired dead zones, this issue was also investigated herein. Considering that the original geometry (Fig. 13) presents corners that can possibly cause undesired effects, two new geometric configurations were evaluated, with curved edges, in order to verify a possible minimization of such problem. The first one was made with a fillet on the

corners, with 0.5 mm, while the second one was built with rounded edge, considering a sector angle of 180º.

Figure 13 - Velocity field at one of the microchannel's edges.

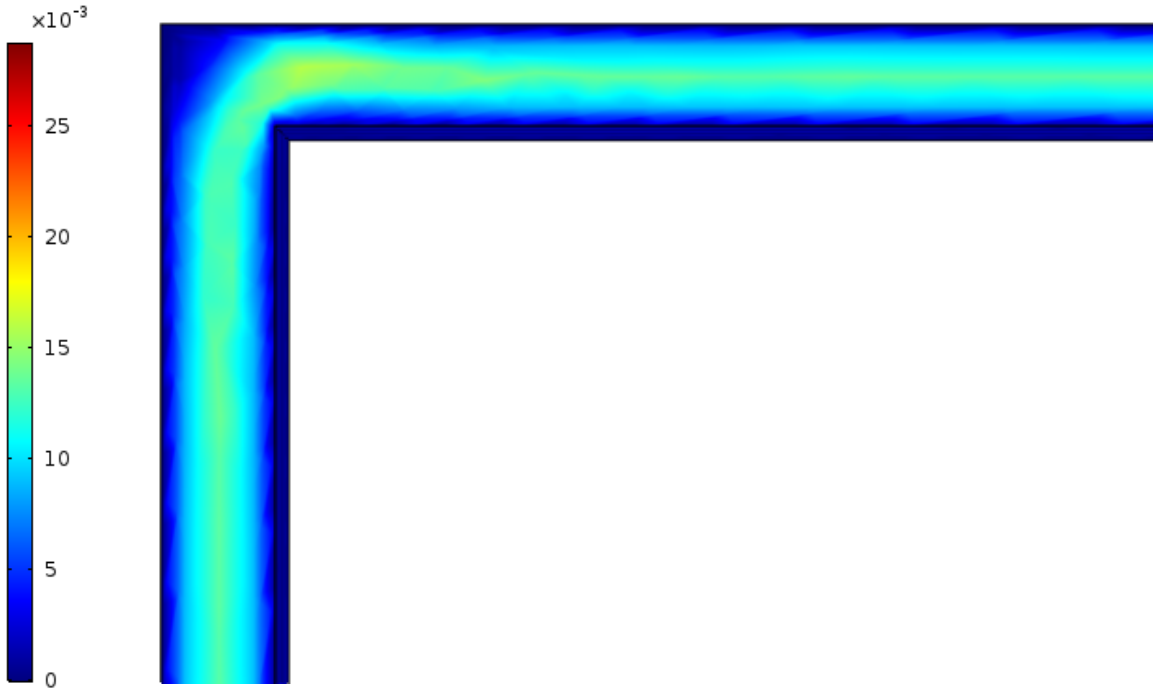

Reference: author (2019).

3.2 RAY-TRACING SIMULATION

The aim of this part of the work is to execute ray-tracing simulations on the LSC-PM. This simulation was made to observe the optical behavior of the system, as a preliminary study for further optimization. To perform this simulation, a commercial ray-tracing software was utilized: LightTools®, version 8.6.0, from Synopsys®. The ray-tracing simulations were based on the Monte Carlo method, allowing to predict the photon distribution in the computational domain. The simulations can be carried out with different ray densities, millions in some cases, depending on the precision desired. The Figure 14 summarize the steps of the ray-tracing simulation of this work.

Figure 14 - Logical flow chart of the ray-tracing simulation.

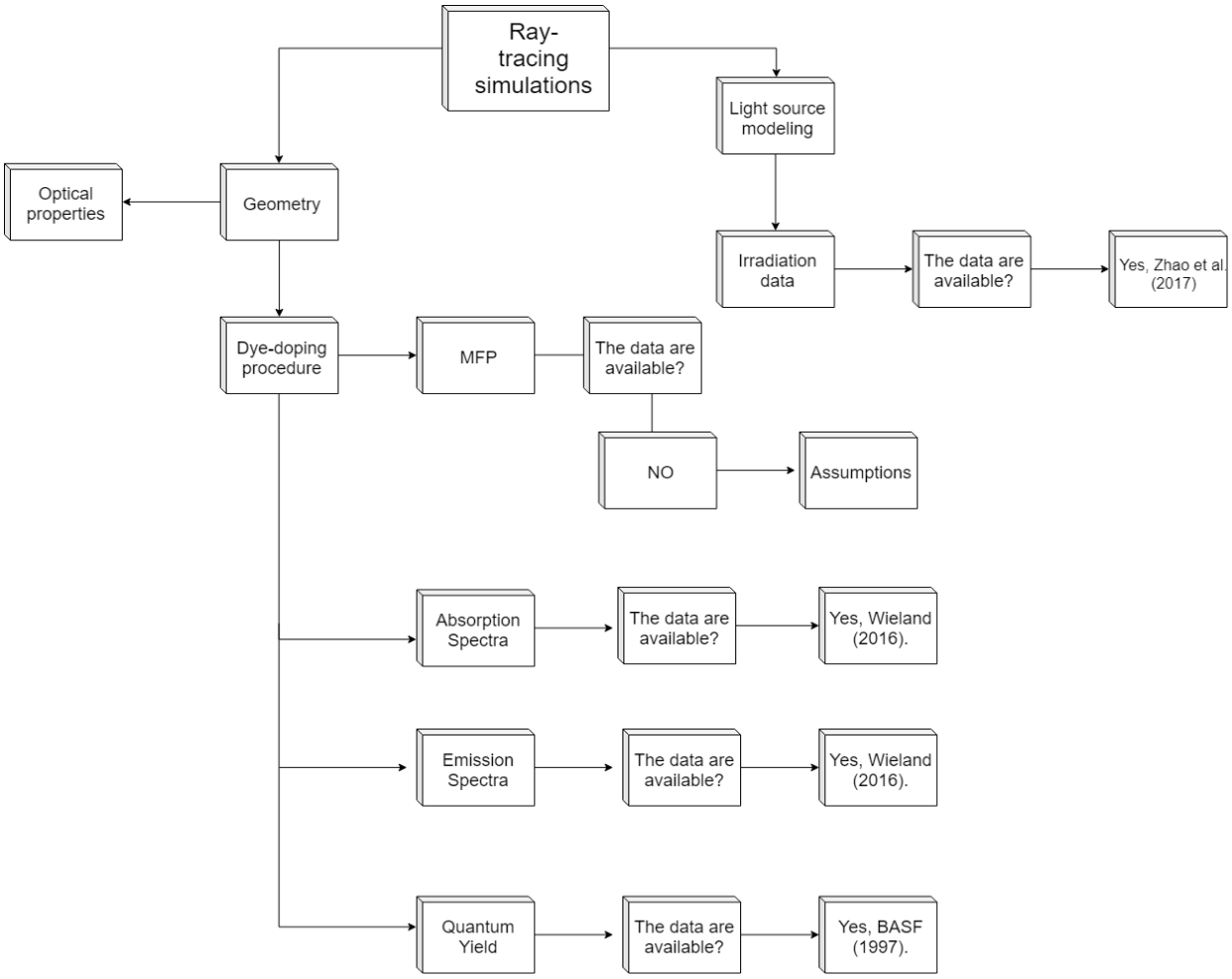

Reference: author (2019).

3.2.1 Geometry

As previously mentioned in section 3.1.1, the model was created with all the features of the original LSC-PM. The geometry was built in three dimensions in the software COMSOL Multiphysics® (version 5.3a), and then imported in the software LightTools® as a CAD file element (Figure 15). The computer used in the optical simulations was the same used in the CFD analysis, running with Intel® Core™ @3.60GHz, 32 GB CPU of RAM and 64-bit Windows operating system.

Figure 15 - Representation of the LSC-PM geometry imported in the software LightTools® (Synopsys®, Inc.).

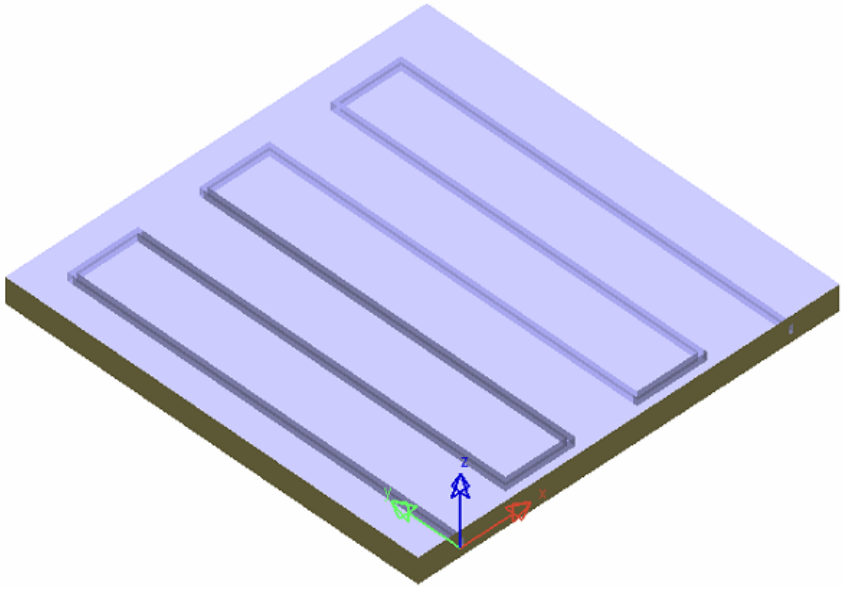

Reference: author (2019).

3.2.1.1 Optical properties

The geometry by itself is not capable to determine the photon distribution on the domain. Thus, one of the most important features in an optical simulation is the setup of the optical properties of the computational domain. Therefore, the first step was the characterization of these geometry's properties. Since the LSC-PM light flux is measured at the edges of the device, the four edges of the waveguide were assigned with 100% absorption. On the other hand, the top and bottom surfaces were defined as Fresnel type, which considers that surface reflections can occur by consequence of the refraction changes in different media (more information about Fresnel losses can be found in the section 2.3.3.2) (MANZANO CHÁVEZ, 2017; SYNOPSYS, 2018b).

3.2.2 Waveguide

As previously stated, the waveguide of the LSC-PM is composed of PDMS, doped with Lumogen F Red 305. The polymer was defined with a constant refractive

index $\mathrm{n} = 1.41$ (WIELAND, 2016), and surrounded by air, with a refractive index $\mathrm{n}_0 = 1.0$. The material was considered as homogeneous, *i.e.*, the refractive index was assumed constant in the computational domain.

The absorption type of the material was set to be defined by the extinction coefficient (k). It represents the imaginary part of light absorbed in a determinate wavelength (SYNOPSYS, 2018a). Eq. 37 can be used to obtain the absorption coefficient and, then, the extinction coefficient can be determined (MANZANO CHÁVEZ, 2017). Considering that in this part only the PDMS by itself (without the dye doping process) is taken into account, a fraction of 10% of the visible light can be considered to be effectively used in the system (WIELAND, 2016). This way, the Eq. (37) uses, consequently, 0.9 as the light transmitted through the material.

$$T = \frac{\phi'}{\phi} = e^{\alpha \cdot d} \tag{37}$$

where T is the transmission, ϕ' is the light transmitted through the material, ϕ is the incident light, α [mm^{-1}] is the absorption coefficient and d is the thickness of the material [mm].

With the values of the thickness of the photomicroreactor, 3 mm, and the transmittance equal to 0.9, an absorption coefficient $\alpha = 0.035\ \mathrm{mm}^{-1}$ was found.

Afterward, the extinction coefficients was calculated through the Eq. (38) (SYNOPSYS, 2018a).

$$k = \frac{\alpha \cdot \lambda}{4 \cdot \pi} \tag{38}$$

where λ is the wavelength.

The values of the extinction coefficient for different wavelengths can be found in Table 2. It was considered that the extinction coefficient is equal to zero for $\lambda \geq 800\ \mathrm{nm}$, *i.e.*, no absorption occurs when this threshold is reached.

Table 2 - Extinction coefficient for the PDMS on different wavelengths.

$\lambda\ [nm]$	k
200	$5{,}57\times10^{-7}$
300	$8{,}35\times10^{-7}$
400	$1{,}1\times10^{-6}$
500	$1{,}39\times10^{-6}$
600	$1{,}67\times10^{-6}$
700	$1{,}94\times10^{-6}$
800	0
900	0

Reference: author (2019).

It is important to highlight that these data are an approximation for non-doped PDMS since that in the LightTools® software it was considered as pure PDMS.

3.2.3 Luminescent particles

The luminescent particles in the LightTools® software are referred to as phosphor due to its capacity to exhibit photoluminescence (ZOLLERS, 2018). Since the PDMS is considered pure in the system, it is necessary to model the phosphor particles of Lumogen F Red 305 dye dispersed in the polymeric device. For accurate modeling, several inputs must be made with the intrinsic characteristics of the dye. The modeling process of phosphors can be summarized in: (1) MFP, (2) absorption spectra, (3) emission spectra, and (4) quantum yield.

3.2.3.1 MFP

The definition of MFP is the average distance (millimeters) that a photon will travel before striking a phosphor particle (SYNOPSYS, 2018a). In this work, the MFP was set as constant, and the excitation input as quantum yield (Stokes Shift calculated when tracing rays).

Considering that the dye concentration and consequently the MFP is unknown in this system, some assumptions were adopted. Chavéz *et al.* (2017) proposed a base case for the MFP with the Red dye 305 in order to analyze its interference on the transport of light. The author varied the MFP in a certain range to observe its interference in the system. In this work, the same assumption was made to observe the system dependence on the MFP.

3.2.3.2 Absorption and emission spectra

The absorption spectrum $\alpha(\lambda)$ can be defined as the wavelength-dependent probability that a photon striking a phosphor be absorbed. This variable ranges from 0 to 1, where 1 indicates 100% of absorption of the photons by the phosphor particles. On the other hand, the emission spectrum is the light intensity emitted by the phosphor particles at different wavelengths (SYNOPSYS, 2018a).

The absorption and emission spectra of the Lumogen F Red 305 were taken from the work of Wieland (2016) are shown in Figure 16. The data was extracted from the plot and a .txt file was generated (with the values presented in Table 3), serving as input in the LightTools® software.

Figure 16 - Absorption and emission spectrum of Red dye 305.

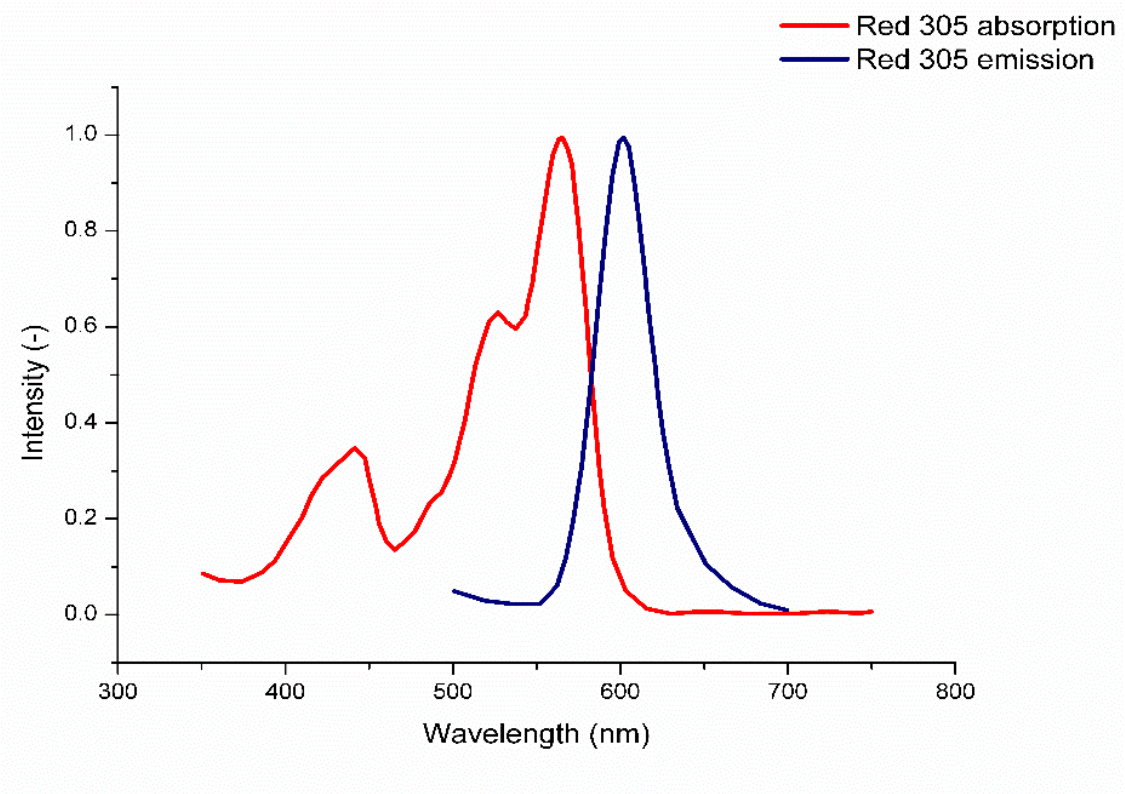

Reference: adapted from Wieland (2016).

3.2.3.3 Quantum yield

The quantum yield is a quantity that defines what fraction of absorbed light of a particular wavelength is re-emitted (ZOLLERS, 2018). BASF has published that the quantum yield of the Red 305 dye is

Table 3 - Emission and absorption spectrum of Red 305 dye at different wavelengths.

	Red 305 absorption spectrum	**Red 305 emission spectrum**
λ $[nm]$	Absorption value	Emission value
350	0.085	-
400	0.151	-
450	0.282	-
500	0.321	0.049
550	0.761	0.022
600	0.050	0.984
650	0.006	0.105
700	0.003	0.009
750	0.002	-

Reference: adapted from Wieland (2016).

98%. Thus, the value, $\mathrm{n_{QY}} = 0.98$, was setup for the absorption range, while for the emission range it was setup as $\mathrm{n_{QY}} = 0$.

3.2.4 Source modeling

Since the final application of the LSC-PM is based on sunlight harvesting, a predictive model should consider the data and region in which the system is run as an input for the optical simulations. LightTools® uses the Meteonorm Meteotest® database for automated input of solar irradiation data. Otherwise, information can be provided as user-defined input when the required time-georeference is not available in the standard database.

The irradiation data for an interval of the day September 29 of 2017 (took as reference, see the Attachment, Table A), and the respective coordinates of Eindhoven, The Netherlands, were obtained from the supplementary data of Zhao *et al.* (2018). Then, the information was inserted in the optical simulation software as a .txt file. The emittance was calculated in the target area, which was defined as rectangular and had the entire photomicroreactor domain selected, immersed on air (ray-tracible). The

spectral region was defined as solar spectral irradiance (AM 1.5) and maintained by default “DirectSunSun_AM1P5SPECTRUM”.

After the input of all the parameters and the analysis of the MFP interference on the system, a variation on the thickness of the photomicroreactor was made in order to observe the influence of this parameter on the energetic performance of the system. The main aim of this step was to characterize the interference of the geometry for further optimization.

Finally, to measure the photon fate in the system, receivers were added in the respective collecting surfaces.

3.2.4.1 Receivers

Three surface receivers were added in the computational domain representing the LSC-PM. The receiver number one was added in the upper surface to measure the incident/absorbed quantity of power on the device. To observe the transmissions losses, a thin plate was built below the device, and a second receiver was inserted on the upper surface of this plate. The third and last receiver was placed in one of the photomicroreactor edges in order to quantify the power reaching on it for further validation of the system with experimental data.

3.2.5 Ray-tracing simulation input

All the simulations run with 2×10^6 rays impinging the system. The deviation of these rays was set up as isotropic, *i.e.*, light can be scattered in all the directions. The random number generator type was set as Sobol, and the ray-path collection was enabled for all the receivers.

4 RESULTS AND DISCUSSION

4.1 CFD SIMULATION

The results obtained numerically were compared with the experimental data for conversion, calculated by Eq. (36), under different conditions (varying the irradiance power and consequently the power collected at a device's edge), in order to validate the computational model.

$$X(\%) = \frac{C_{in} - C_{out}}{C_{in}} \times 100 \tag{36}$$

Figure 17 shows a comparison between the simulated results and the experimental data for the DPA conversion over time considering constant light irradiation on the LSC-PM's surface at different levels (leading to tip power equal to 0.01, 0.058, 0.093, 0.17, 0.30 and 0.48 W). The results indicated that the model presents excellent agreement with the experimental data, with maximum error < 13%. Thus, it can be stated that the proposed computational model adequately represents the conversion of DPA under different light intensities.

Additionally, it can be observed that at low powers (0.01 W), the DPA conversion was only about 45%. However, for the tip power of 0.48 W a conversion as high as 94% was observed even with very low residence times. For P = 0.058 W, conversions up to 95% can be also achieved, although it requires residence times ~9x higher than that adopted for higher light intensities.

One of the limitations of using sunlight in chemical reactions is the oscillation of the magnitude of light during the day, *e.g.*, cloudy days, rainy days and even clouds passing on sunny days. In such cases, there is a reduction in the efficiency of the reaction unit. Therefore, to avoid this oscillation, a feedforward control can be applied to maintain the DPA conversion constant in a desired set-point, as mentioned in section 2.2.

Initially, the reactor was submitted to the power of 0.48 W for 20 s. Afterward, the power was decreased to 0.01 W also for 20 s (to represent the passage of a cloud if using sunlight). Again, the power was increased to 0.48 W, using the rectangular function, and the process was repeated cyclically until the final time of 200 s was reached.

Figure 17 - Comparison between experimental data and those obtained by the numerical simulations.

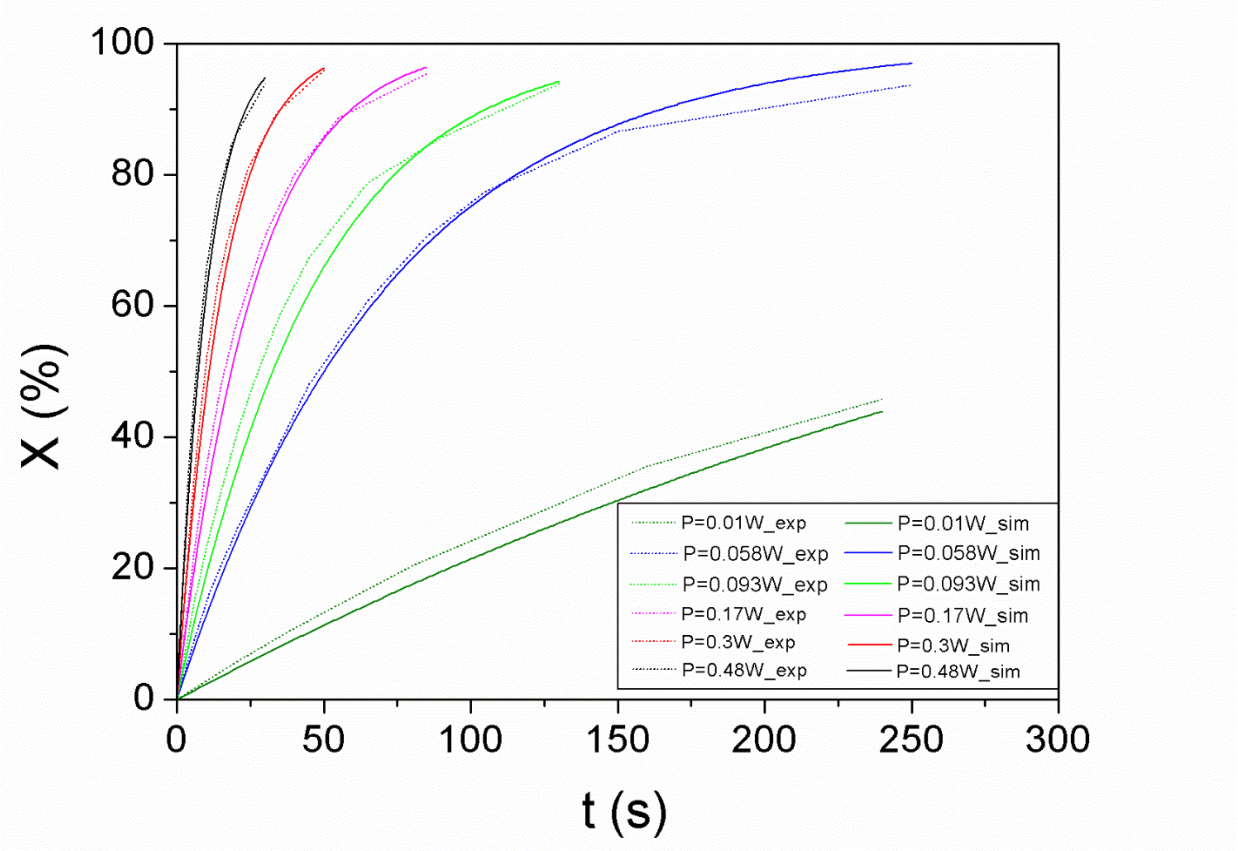

Reference: author (2019).

Fig. 18 shows the difference observed for the process with and without the control system during power disturbances. It can be clearly seen that when the control system is disabled, the conversion decreases drastically (from ~80% to < 10%) due to the reduction in light intensity. Additionally, it can be also observed that in the case where there is no control, the DPA conversion did not even get close to the conversion target value. However, the opposite behavior was observed when the feedforward

control system was implemented. Once enabled, the control system was able to maintain the conversion at the level of 90% (set-point) even during the drastic disturbances performed.

However, it is of paramount importance, given the precision expected when operating microfluidic devices, that the dead time resulting from the control action (reading the LSC-PM's tip power and acting on the pump to adjust the velocity at the inlet, and consequently the residence time) is negligible. Significant time delays can harmfully affect the response of the process in a way that can make unfeasible the application of photomicroreactors for the synthesis of added-value compounds (such as pharmaceuticals active agents and intermediates, food additives, etc.). The time delay found in the experimental setup of the LSC-PM investigated herein was nearly 0.5 s, resulting in a real-time control (ZHAO *et al.*, 2018) the validated CFD model, though, one can now evaluate the dangerous impact of higher dead times on the system's performance.

Figure 18 - Comparison of LSC-PM reactor with and without conversion control, considering 90% as target conversion.

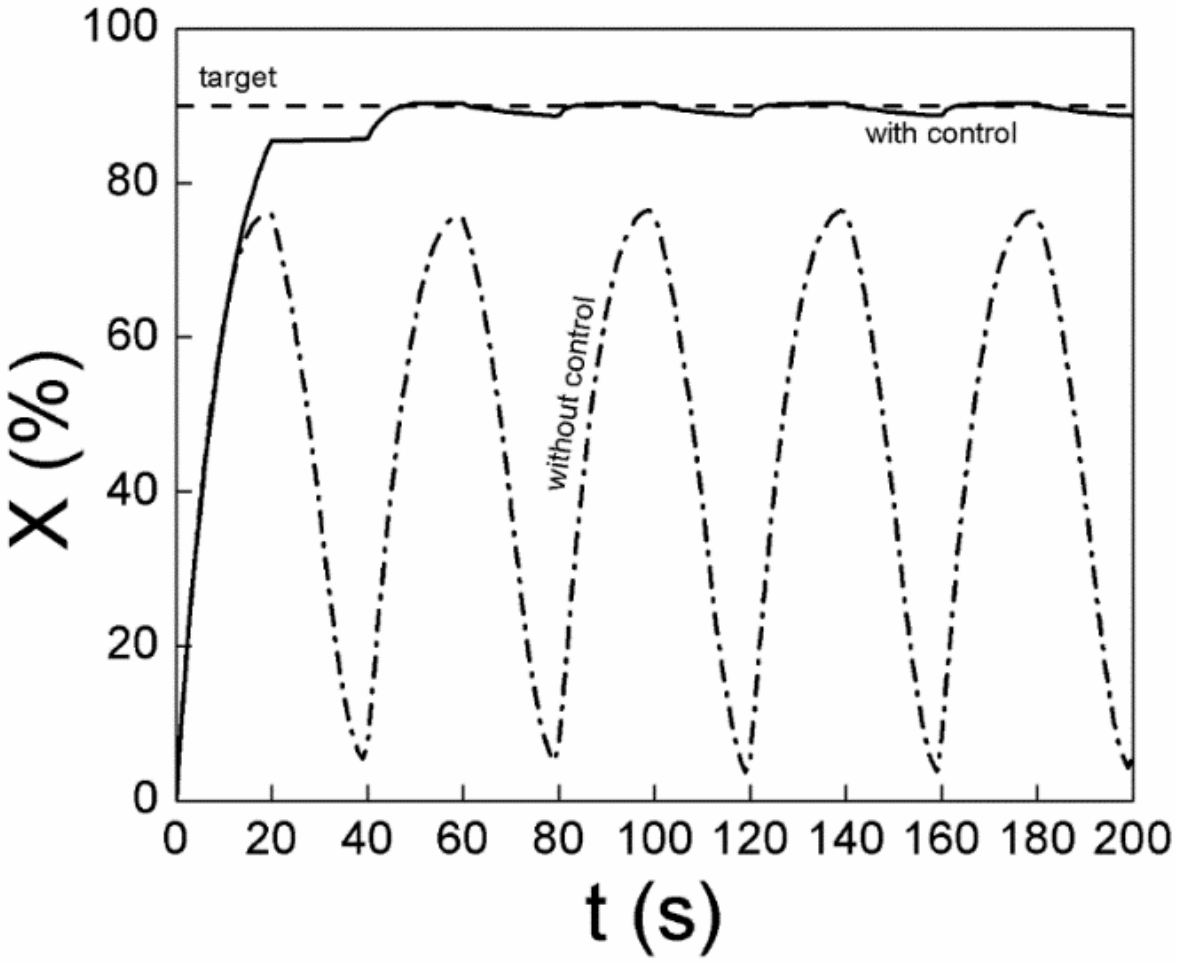

Reference: author (2019).

Fig. 19 shows the three functions used to impose variations in the light intensity (rectangular, triangular and sinusoidal) with different time delays (0.5, 1, 5 and 10 s). Qualitatively, the difference in the system response for the delays of 0.5 and 1 s is almost indistinguishable. Nevertheless, substantial differences were notices for time delays higher than 5 s. Clearly, it can be noticed that the delay of 10 s (the higher evaluated) presented greater deviations from the set-point for conversion considering all the three functions tested. In addition, for the rectangular disturbance (Fig. 19a), the conversion reduced to 80% when the tip power decreases from 0.48 W to 0.01 W,

considering a delay of 10 s. However, for the other function formats (triangular and sinusoidal), the conversion did not decrease so drastically.

This behavior can be explained due to the fact that when a sudden decrease in light intensity occurs without an immediate decrease of the flow rate the result is a decrease in the reaction rate and, consequently, in the species conversion. Therefore, it seems reasonable to assume that the delay evaluation is of paramount importance for the proper design of the control system.

Quantitatively, it was possible to evaluate the control performance for the different time delays based on the performance indices: integral absolute error (IAE), integral square error (ISE) and integral of time multiplied absolute error (ITAE), according to Eq. (37) to (39), respectively.

$$IAE = \int_0^t |r(t) - y(t)| \tag{37}$$

$$ISE = \int_0^t \big(r(t) - y(t)\big)^2 \tag{38}$$

$$IAE = \int_0^t t \cdot |r(t) - y(t)| \tag{39}$$

where $r(t)$ is the reference value, corresponding to the set-point (X = 90%) and $y(t)$ is the response of the photomicroreactor. Table 4 presents the evaluation criteria for delays of 0.5, 1, 5 and 10 s. According to these criteria, the performance of the control will be better the lower the values of the integral errors. As expected, it is verified that the delay of 0.5 s presented the best results for all the criteria used (low values) and also for all the formats of the variations of the power. In addition, the delay of 10 s presented higher values for all criteria, thus representing a poor performance of the controller with this delay. These effects can also be observed qualitatively in Fig. 19.

Another important point to follow is the flow behavior in the microreactor. Considering that the rectangular junctions of the microchannels can result in a nonideal

scenario, the CFD model was used to investigate the reactor's performance with rounded junctions. The results obtained are highlighted in Figure 20.

Figure 19 - Comparative evaluation for different time delays for power format: (a) rectangular, (b) triangular and (c) sinusoidal.

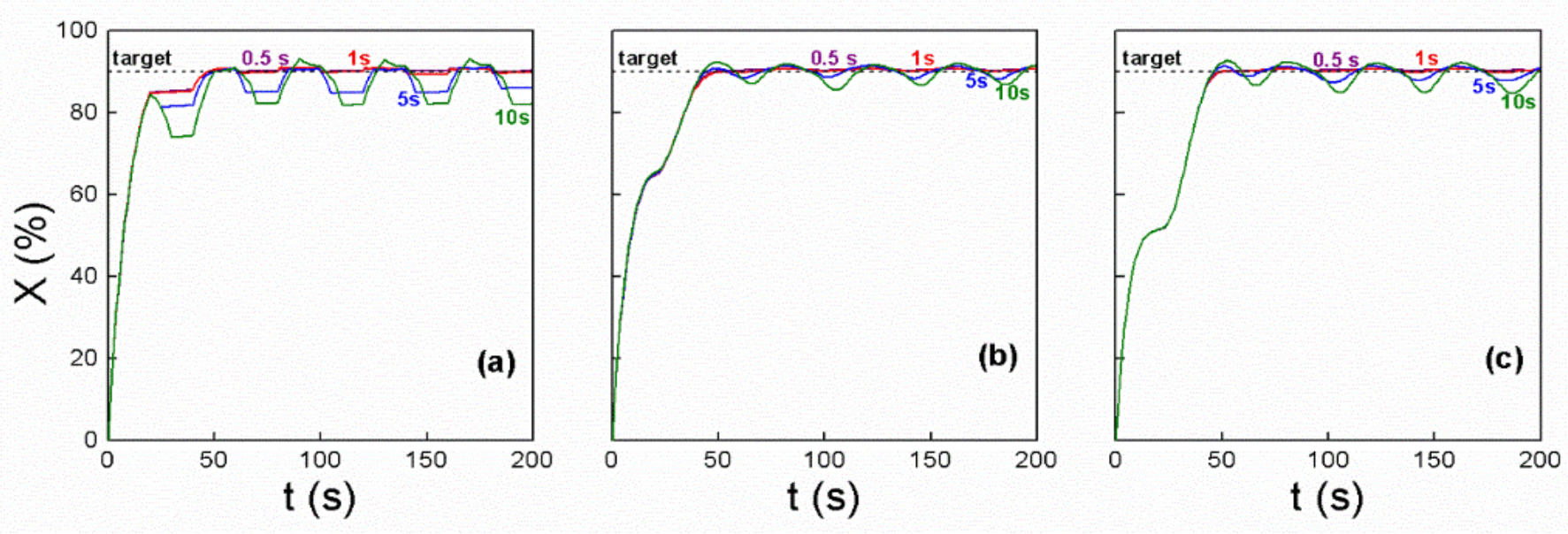

Reference: author (2019).

Table 4 - Error performance for different time delays in the LSC-PM control system.

	Rectangular			Triangular			Sinusoidal		
	IAE	ISE	ITAE	IAE	ISE	ITAE	IAE	ISE	ITAE
0.5 s	9.07×10^{2}	4.02×10^{4}	1.53×10^{4}	1.29×10^{3}	5.40×10^{4}	2.40×10^{4}	1.67×10^{3}	7.56×10^{4}	3.14×10^{4}
1 s	9.24×10^{2}	3.99×10^{4}	1.77×10^{4}	1.31×10^{3}	5.48×10^{4}	2.48×10^{4}	1.68×10^{3}	7.56×10^{4}	3.32×10^{4}
5 s	1.31×10^{3}	4.24×10^{4}	5.99×10^{4}	1.36×10^{3}	5.42×10^{4}	3.23×10^{4}	1.77×10^{3}	7.57×10^{4}	4.48×10^{4}
10 s	1.61×10^{3}	4.69×10^{4}	8.88×10^{4}	1.46×10^{3}	5.43×10^{4}	4.49×10^{4}	1.93×10^{3}	7.65×10^{4}	6.55×10^{4}

Reference: author (2019).

Figure 20 - Velocity field in three different geometries: (a) original, (b) slightly curved and (c) highly curved.

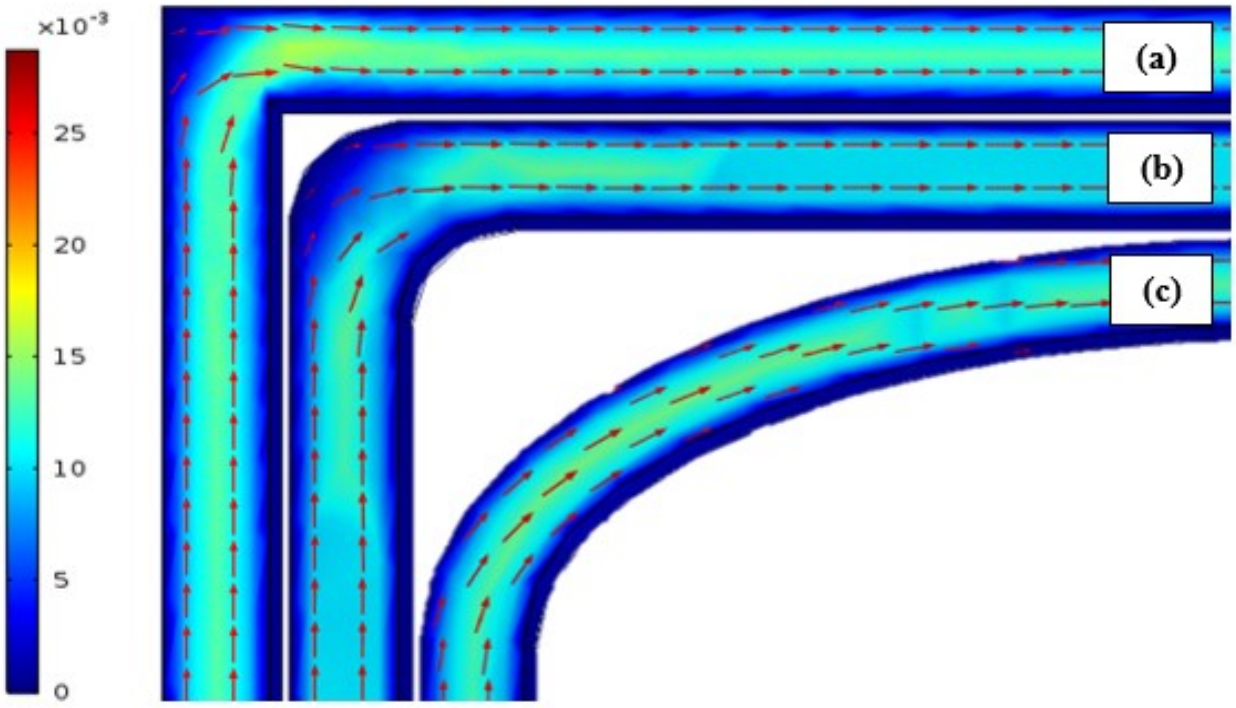

Reference: author (2019).

From the results obtained in Fig. 20, it is possible to observe that in the second geometry (b) the behavior was quite similar to the original geometry (a). However, in the third geometry tested (c), a considerable change was observed when compared to the original geometry, the low velocity zones in the corners are no longer visible, since the corners are now curved. Nonetheless, an important parameter to observe is the conversion in all the geometries. Then, a percentual error between the conversions was made. As expected, the geometry (c) was the one that resulted in higher deviation in the conversion from the initial geometry, with the value of 91.27% of conversion, while the geometry (a) reached a conversion of 90.67% (Δ of ~0.65% between them). Meanwhile, geometry (b) resulted in a conversion of 90.96%, not so different from the performance obtained with the original geometry (Δ of ~0.31%). Thus, the original geometry, although based on rectangular corners, showed an acceptable behavior

when compared with the new geometries taking the minimal difference in DPA conversion into account.

4.2 RAY-TRACING SIMULATION

The optical analysis was conducted by first observing the power distribution on the system. This was carried out through the ray-tracing of 2×10^6 rays impinging the device's top surface. This number of rays was chosen to improve the accuracy of the simulations. The surface receiver number one, located on the top of the photomicroreactor, collected 3,904,270 samples. Thus, the total incident power collected by this face was 1.771 W, and only 0.117 W was absorbed by the microchannels, with an error at peak estimated in 0.10%. This decrease in the power can be a consequence of the reflection or transmission losses in the system. To quantify the losses by transmission, a thin plate was placed under the photomicroreactor ($\mathrm{z} = -10\,\mathrm{mm}$), with a receiver on it. The representation of the system after the ray-tracing simulation and the thin plate bellow the photomicroreactor can be seen in Figure 21.

Figure 21- Ray-tracing simulations in the LightTools® software*: (a) Ray-tracing simulation on the LSC-PM, (b) Ray-tracing simulation with a thin plate under the LSC-PM.

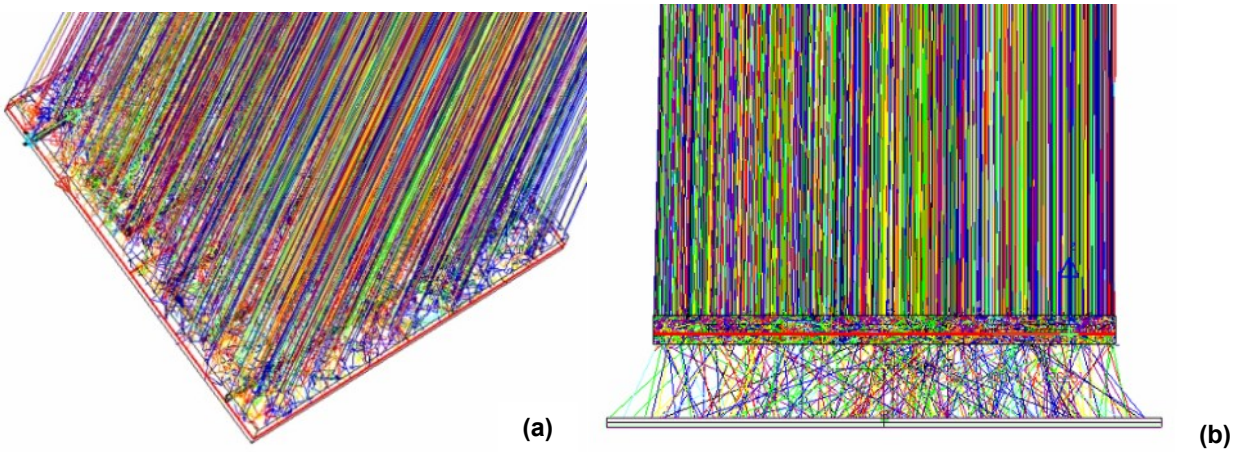

(a) **(b)**

Reference: author (2019). *The ray-tracing simulations were made in this representation with 10,000 rays to facilitate the visualization of the rays in the system.

As a result of the transmission evaluation, receiver number three indicates that 0.058 W of power was lost by transmission. The error at the peak was of 1.46% and the number of samples read was 237,425. However, since the light source is the sun, and the insertion of a plate above the reactor (even with transmitted optical properties) don't result in a measure exclusively of the reflected rays, the reflection losses are not able to be elucidated in this case.

As already stated by Zhao *et al.* (2018), the power measured at the device's edges can be considered proportional to the power on the channels. Based on that, the power output at the edges was collected in order to make a further validation of the system with experimental data in the near future. At this moment, the output edge power can be considered as a guide for the evaluation of the energy losses within the system. Therefore, the receiver number two (placed on the edge of the phomicroreactor), read a total of 43,133 samples. The power output obtained was 0.0183W, with an error at peak of 3.40%. Accordingly, and considering that the power of 0.117W was within the system, the percentage of rays that ended up reaching the edge was about 7.39% (considering 100% of absorption on the edges).

In the sequence, an MFP analysis was carried out. As previously mentioned in item 3.2, the MFP is unknown a priori. Then, when the simulation was set up, the MFP was varied in a wide range (0.1 – 20) mm to observe the influence of this parameter on the system's performance. The range (0.1 – 1) mm was varied with an interval of 0.1 mm, the range (1 – 10) mm was varied with increment of 1 mm and, finally, the interval (10 – 20) mm was varied with a step of 5 mm. The response of the system can be observed in Figure 22, and the respective power values and the number of samples can be encountered in Table B1 in Appendix B.

From Figure 22, it seems reasonable to consider that the MFP influences the energy distribution in the system. Its response on the power distribution is a consequence of different factors. Incident photon flux, power absorption and power output at the device's edges are closely related.

An interesting behavior relating incident and absorbed power can be observed in Figure 22. The increase in the absorption of photons by the system can be explained by the decrease of the self-absorption losses. In other words, when in high

concentration, the phosphor particles absorb the photons and no longer re-emit them. This observation is in accordance with the work of Krumer *et al.* (2017), who stated that high concentration of phosphor particles in the system (in this case $\mathrm{MFP} < 1\ mm$) has negative effect on the performance of the device when photon re-emission is the target.

Figure 22 - MFP influence on the energetic efficiency of the LSC-PM.

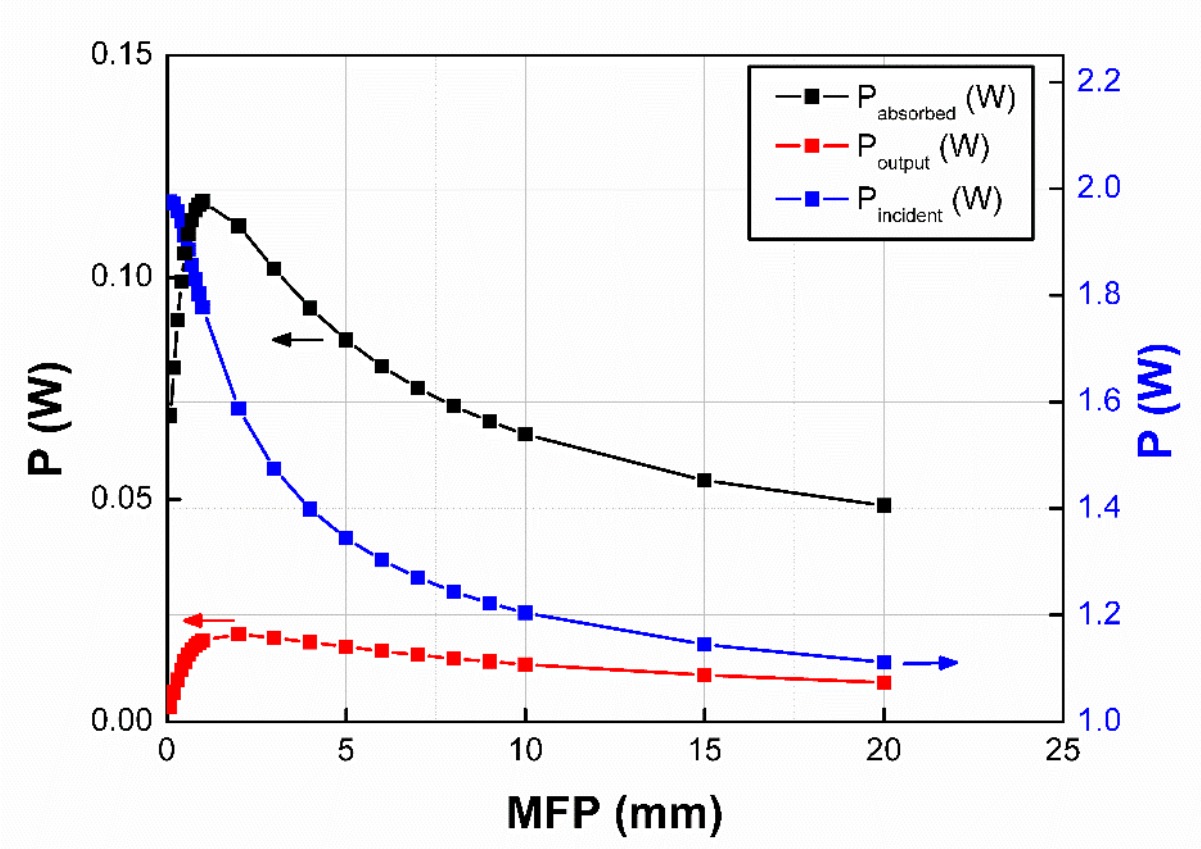

Reference: author (2019).

Figure 22 also clearly shows, as expected, that the edge output power increases as the power within the system is higher. From the simulations it was possible to notice that the peak of power within the system was reached when $\mathrm{MFP} \approx 1\ \mathrm{mm}$. An increase in the MFP up to 20 mm resulted in a reduction on the power absorption and in the power output. The main reason for this decrease is the high transmission on the system. Chavéz (2017), affirms that the low concentration of phosphor particles generates an open area allowing the photons to pass through the

device, which justifies the power decrease with larger MFP. Another reason can be the scattering effects, which according to Hwang *et al.* (2014), are more pronounced in lower dye concentrations and, occasionally, these scattering effects can guide the light outside the device (SCHRECENGOST *et al.*, 2018).

Thus, from the observation on the behavior of the system with varying MFP, an MFP of 1 mm can be considered ideal. Thus, all the simulations in this work were carried out with this MFP. Further experimental work with varying dye concentrations should be carried out to reach this MFP in order to validate the observations presented herein and, therefore, optimize the device's performance.

Finally, a preliminary modification on the geometry was made to observe the effect of the LSC's thickness on the photon distribution in the system. The response in terms of power absorbed and power collected at the device's edge for three distinct thicknesses are presented in Figure 23.

Figure 23 - Influence of the waveguide thickness on the system's power distribution.

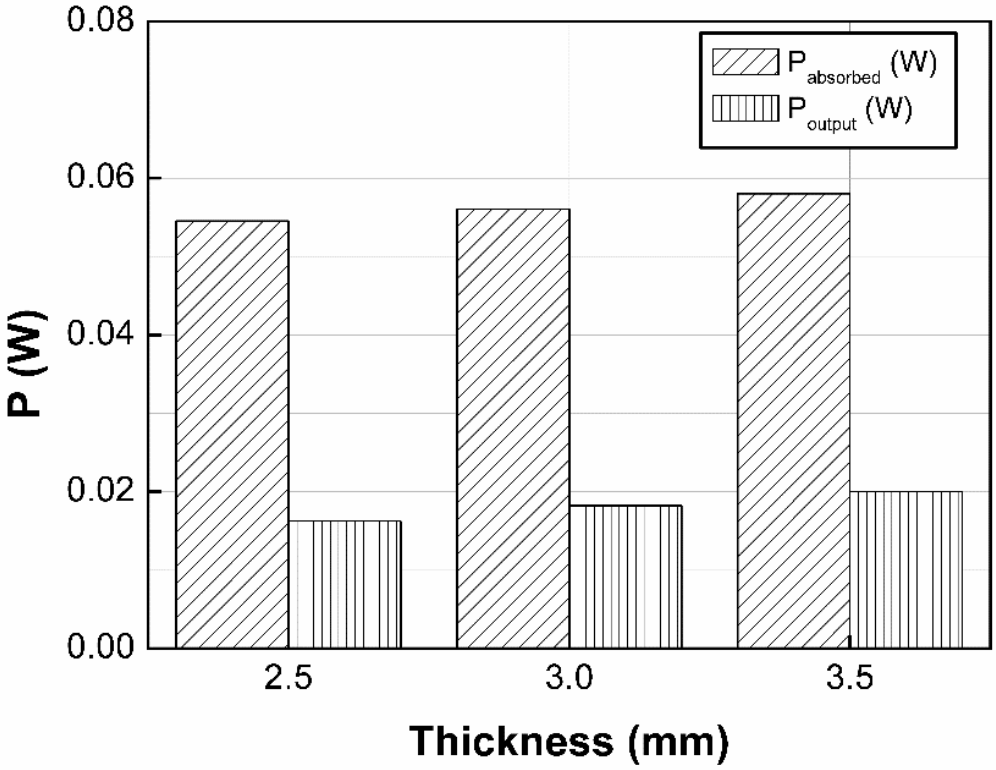

Reference: author (2019).

Thus, the geometric configuration of the LSC-PM influences not only the fluid dynamics within the microchannels but also the optical performance of the system. Figure 23 shows that a slight increase in the power absorbed as well as in the power output (at the LSC-PM's edges) occurs when the thickness of the lightguide is also increased. This fact can be explained due to the decrease in the transmission through the system, since the chance of trapping the photons is higher as the thickness of the lightguide is increased. Additional studies will be carried out to analyze the behavior of the device under different geometric configurations, in order to consider scale-out strategies for this system.

5 CONCLUSIONS

This study highlighted that CFD can be successfully applied to the investigation of fluid dynamics in a microreactor. The CFD model developed showed a good agreement in the temporal analysis of the conversion on different powers when compared to the experimental data, making possible the validation of the model. The feedforward system that was implemented in the reaction system was able to maintain the conversion at the target value despite the changes of the light irradiation, where the best configuration of the control system occurred with the delay of 0.5 seconds, a real-time control proved to be realizable. Moreover, the original geometry showed good behavior when the conversion was studied, proving no need for change on it.

From the optical simulation, it was possible to elucidate the energy that reaches within the system by the fate of the photons. The power that reaches the top of the device and the output power could be collected as well. The investigation on the losses proved that some optimization still can be made to improve the system's performance (*e.g.* geometry optimization). However, further investigations must be done to elucidate all the losses. The validation is the principal next step, having in mind that in order to make the optimization, the simulations must have a good agreement with the experimental data.

This study served as an initial point for further developments within our research group towards a fully coupled model integrating CFD and optical simulations for the evaluation of the LSC-PM performance under different scenarios, a step required for the proposition of scale-out strategies for this system as well as for the energetic optimization of the device.

6 RECOMMENDATIONS FOR FUTURE WORK

The following topics constitute improvements to be added to this work in order to improve the predictive performance of the computational model developed for the LSC-PM:

- validation of the optical performance of the device harvesting sunlight using experimental data under outdoor conditions.
- simulation and validation of the optical performance of the device irradiated with led strips.
- coupling the CFD model with the optical model, taking the light input for the chemical kinetics from the photon flux reaching the microchannels considering all the optical phenomena occurring in this device.
- verification on the performance of the software LightTools® when compared to other commercial available tools.
- investigation on scale-out strategies for this system based on the CFD/optical coupled computational model.
- investigation in performances of the control system under a random scenario of light intensity fluctuation.
- investigation in performances of different advanced control strategies.
- integration of CFD/optical model with doe (design of experiments) and ai (artificial intelligence).
- optimization of the LSC-PM in terms of optics and fluid flow considering complete coupling of all phenomena involved.

REFERENCES

AIDA, Shin *et al.* Microflow photochemistry — a reactor comparison study using the photochemical synthesis of terebic acid as a model reaction. **Tetrahedron Letters**, v. 53, n. 42, p. 5578–5581, 2012. Available in: <http://dx.doi.org/10.1016/j.tetlet.2012.07.143>.

AKWI, Faith M.; WATTS, Paul. Continuous flow chemistry: where are we now? Recent applications, challenges and limitations. **Chem. Commun.**, p. 13894–13928, 2018.

ANGNES, Ricardo A. *et al.* Recent synthetic additions to the visible light photoredox catalysis toolbox. **Org. Biomol. Chem**., v. 13, n. 35, p. 9152–9167, 2015. Available in: <http://xlink.rsc.org/?DOI=C5OB01349F>.

APAKONSTANTINOU, P. Flexible and fluorophore-doped luminescent solar concentrators based on polydimethylsiloxane. **Optics Letters.** v. 41, n. 4, p. 713–716, 2016.

ASAHI, R. Visible-Light Photocatalysis in Nitrogen-Doped Titanium Oxides. **Science.** v. 269, n. 2001, 2012.

ATHANAILEAS, T E *et al.* Parallel radio-wave propagation modeling with image-based ray tracing techniques. **Parallel Computing**, v. 36, n. 12, p. 679–695, 2010. Available in: <http://dx.doi.org/10.1016/j.parco.2010.08.002>.

BALABAN, Benjamin L. **The Role Of Förster Resonance Energy Transfer In Luminescent Solar Concentrator Efficiency And Color Tunability**. 2013.

BASF, **Lumogen F - Collector dyes.** November, 1997.

BHAGAT, Ali Asgar S; JOTHIMUTHU, Preetha; PAPAUTSKY, Ian. Photodefinable polydimethylsiloxane (PDMS) for rapid lab-on-a-chip prototyping. **Lab on a Chip,** p. 1192–1197, 2007.

BIRD, R. Byron; STEWART, Warren E.; LIGHTFOOT, Edwin N. **Transport Phenomena.** Second Ed. John Wíley & Sons, Inc., 2007.

BRYDSON, **To John A. Dedication Brydson ' s Plastics Materials,** 2017.

CAMBIÉ, Dario *et al.* A Leaf-Inspired Luminescent Solar Concentrator for Energy-Efficient Continuous-Flow Photochemistry. **Angewandte Chemie - International Edition**, v. 56, n. 4, p. 1050–1054, 2017a.

CAMBIÉ, Dario *et al.* Applications of Continuous-Flow Photochemistry in Organic Synthesis, Material Science, and Water Treatment. **Chemical Reviews**, v. 116, n. 17,

p. 10276–10341, 2016.

CAMBIÉ, Dario *et al.* Every photon counts: understanding and optimizing photon paths in luminescent solar concentrator-based photomicroreactors (LSC-PMs). **React. Chem. Eng.**, v. 2, n. 4, p. 561–566, 2017b. Available in: <http://xlink.rsc.org/?DOI=C7RE00077D>.

CAMBIÉ, Dario *et al.* Every photon counts: Understanding and optimizing photon paths in luminescent solar concentrator-based photomicroreactors (LSC-PMs). **Reaction Chemistry and Engineering**, v. 2, n. 4, p. 561–566, 2017c.

CELIK, Ismail B. *et al.* Procedure for Estimation and Reporting of Uncertainty Due to Discretization in CFD Applications. **Journal of Fluids Engineering,** v. 130, n. July 2008, p. 5–8, 2008.

CHEN, Zhongqiang; DELIS, Alex; BERTONI, Henry L. Radio-wave propagation prediction using ray-tracing techniques on a network of workstations (NOW). **Journal of Parallel and Distributed Computing,** v. 64, p. 1127–1156, 2004.

CHETVERUSHKIN, B *et al.* Development of a CFD-Based Model for Photo-Reactor Simulation. **Parallel Computational Fluid Dynamics - Advanced Numerical Methods, Software and Applications,** p. 243–250, 2004.

CHOU, Chun Hsien; CHUANG, Jui Kang; CHEN, Fang Chung. High-performance flexible waveguiding photovoltaics. **Scientific Reports,** v. 3, 2013.

CHOU, Chun Hsien; HSU, Min Hung; CHEN, Fung Chung. Flexible luminescent waveguiding photovoltaics exhibiting strong scattering effects from the dye aggregation. **Nano Energy**, v. 15, p. 729–736, 2015. Available in: <http://dx.doi.org/10.1016/j.nanoen.2015.06.001>.

CIANA, Claire-Lise; BOCHET, Christian G. Clean and Easy Photochemistry. **Photochemistry**, 2007.

CLENNAN, Edward L.; PACE, Andrea. Advances in singlet oxygen chemistry. **Tetrahedron**, v. 61, n. 28, p. 6665–6691, 2005.

COMMENGE, J M *et al.* Optimal Design for Flow Uniformity in Microchannel Reactors. **AIChE Journal**, v. 48, n. 2, 2002.

COMSOL. **COMSOL Multiphysics® User's Guide**, 2012.

CORRADO, Carley *et al.* Solar Energy Materials & Solar Cells Optimization of gain and energy conversion efficiency using front-facing photovoltaic cell luminescent solar concentrator design. **Solar Energy Materials and Solar Cells,** v. 111, p. 74–81, 2013. Available in: <http://dx.doi.org/10.1016/j.solmat.2012.12.030>.

COYLE, Emma E.; OELGEMÖLLER, Michael. Micro-photochemistry: photochemistry in microstructured reactors. The new photochemistry of the future? **Photochemical & Photobiological Sciences,** v. 7, n. 11, p. 1313, 2008. Available in: <http://xlink.rsc.org/?DOI=b808778d>.

DAS, Anshuman J; NARAYAN, K S. Retention of Power Conversion Effi ciency – From Small Area to Large Area Polymer Solar Cells. **Advanced Materials,** p. 2193–2199, 2013.

DEBIJE, Michael G. Solar energy collectors with tunable transmission. **Advanced Functional Materials**, v. 20, n. 9, p. 1498–1502, 2010.

DEBIJE, Michael G.; VERBUNT, Paul P.C. Thirty years of luminescent solar concentrator research: Solar energy for the built environment. **Advanced Energy Materials**, v. 2, n. 1, p. 12–35, 2012.

DEROSA, Maria C.; CRUTCHLEY, Robert J. Photosensitized singlet oxygen and its applications. **Coordination Chemistry Reviews**, v. 233–234, p. 351–371, 2002.

DESMET, L *et al.* Monocrystalline silicon photovoltaic luminescent solar concentrator with 4 . 2 % power conversion efficiency. **Optics Letters,** v. 37, n. 15, p. 3087–3089, 2012.

DIENEL, Thomas *et al.* Spectral-based analysis of thin film luminescent solar concentrators. **Solar Energy,** v. 84, p. 1366–1369, 2010.

DING, F; WAN, W; YUAN, H. The infuence of background winds and attenuation on the propagation of atmospheric gravity waves. **Journal of Atmospheric and Solar-Terrestrial Physics,** v. 65, p. 857–869, 2003.

EBRAHIMIPOUR, Bahareh Alsadat; ASKARI, Hassan Ranjbar; RAMEZANI, Ali Behjat. Investigation of linear optical absorption coefficients in core-shell quantum dot (QD) luminescent solar concentrators (LSCs). **Superlattices and Microstructures,** v. 97, p. 495–505, 2016. Available in: <http://dx.doi.org/10.1016/j.spmi.2016.07.011>.

ERICKSON, Christian S *et al.* Zero-Reabsorption Doped-Nanocrystal Luminescent Solar Concentrators. **ACS Nano,** n. 4, p. 3461–3467, 2014.

FABRY, David C; SUGIONO, Erli; RUEPING, Magnus. Self-Optimizing Reactor Systems: Algorithms , On-line Analytics , Setups , and Strategies for Accelerating Continuous Flow Process Optimization. **Israel Journal of Chemistry,** n. 0, p. 341–350, 2014.

FITZPATRICK, Daniel E; BATTILOCCHIO, Claudio; LEY, Steven V. Enabling Technologies for the Future of Chemical Synthesis. **ACS Central Science,** 2016.

GOETZBERGER, A.; GREUBEL, W. **United States Patent,** n. 19, 1978.

GOETZBERGER, A; GREUBEL, W. Solar Energy Conversion with Fluorescent Collectors. **Applied Physics,** v. 139, 1977.

GRIFFINI, Gianmarco; ASTERIOS, Gavriilidis. Effect of Microchannel Plate Design on Fluid Flow Uniformity at Low Flow Rates. **Chem. Eng. Technol,** n. 3, p. 395–406, 2007.

GRUNBERG, L.; NISSAN, A.H. Mixture Law for Viscosity. **Nature,** v. 164, p. 799–900, 1949.

Ghosh, T. (2016). Visible Light-Induced Reductive Photoredox Catalysis in Organic Synthesis. *Universität Regensburg*, (**Dissertation**), 187.

Haines, C., Chen, M., & Ghiggino, K. P. (2012). The effect of perylene diimide aggregation on the light collection efficiency of luminescent concentrators. ***Solar Energy Materials and Solar Cells***, *105*, 287–292. https://doi.org/10.1016/j.solmat.2012.06.030

HARI, Durga Prasad; KO, Burkhard. Synthetic applications of eosin Y in photoredox catalysis. **Chem. Commun.,** p. 6688–6699, 2014.

HOFMANN, Oliver *et al.* Monolithically integrated dye-doped PDMS long-pass filters for disposable on-chip fluorescence detection. **Lab on a Chip,** p. 981–987, 2006.

HU, Xiangmin *et al.* Ray-trace simulation of CuInS $(Se)_2$ quantum dot based luminescent solar concentrators. **Optics Express,** v. 23, n. 15, p. 163–169, 2015.

ILAN, Boaz; KELLEY, David F. Photon Transport in Luminescent Solar Concentrators based on Semiconductor Nanoparticles. **Renewable Energy and the Environment Technical Digest,** p. 12–14, 2011.

JANG, Hyoseon; HOPKINS, Carl. Prediction of sound transmission in long spaces using ray tracing and experimental Statistical Energy Analysis. **Applied Acoustics,** v. 130, p. 15–33, 2018. Available in: <https://doi.org/10.1016/j.apacoust.2017.09.004>.

JI, Xiangfei; ZHANG, Yiqun. Solar ray collection rate fluctuation analysis with Monte Carlo Ray Tracing method for space solar power satellite. **Solar Energy,** v. 185, n. 2, p. 235–244, 2019. Available in: <https://doi.org/10.1016/j.solener.2019.04.067>.

JONES, R Michael; BEDARD, Alfred J. Atmospheric gravity wave ray tracing : Ordinary and extraordinary waves. **Journal of Atmospheric and Solar-Terrestrial Physics,** v. 179, n. August, p. 342–357, 2018. Available in: <https://doi.org/10.1016/j.jastp.2018.08.014>.

KABIR, Ehsanul *et al.* Solar energy: Potential and future prospects. **Renewable and Sustainable Energy Reviews,** v. 82, n. September 2017, p. 894–900, 2018.

KALAITZAKIS, Dimitris *et al.* Methylene Blue as a Photosensitizer and Redox Agent : Synthesis of 5-Hydroxy-1 H -pyrrol-2 (5 H) -ones from Furans ** **Angewandte Chemie,** n. 277588, p. 6283–6287, 2015.

KAOARNOS, George J. **Fundamentals of Photoinduced Electron Transfer,** 1993.

KÇNIG, B *et al.* The Photocatalyzed Meerwein Arylation: Classic Reaction of Aryl Diazonium Salts in a New Light. **Angewandte Minireviews,** n. Ii, p. 4734–4743, 2013.

KERROUCHE, A. *et al.* Luminescent solar concentrators: From experimental validation of 3D ray-tracing simulations to coloured stained-glass windows for BIPV. **Solar Energy Materials and Solar Cells,** v. 122, p. 99–106, 2014. Available in: <http://dx.doi.org/10.1016/j.solmat.2013.11.026>.

KRUK, Irena. **The Handbook of Environmental Chemistry,** 1998.

KRUMER, Zachar *et al.* Compensation of self-absorption losses in luminescent solar concentrators by increasing luminophore concentration. **Solar Energy Materials and Solar Cells,** v. 167, n. July 2016, p. 133–139, 2017. Available in: <http://dx.doi.org/10.1016/j.solmat.2017.04.010>.

KRUMER, Zachar *et al.* Solar Energy Materials & Solar Cells Tackling self-absorption in luminescent solar concentrators with type-II colloidal quantum dots. **Solar Energy Materials & Solar Cells,** v. 111, p. 57–65, 2013.

Kumar, H., Velu, R., & Balasubramanian, E. (2019). A novel freeform lens design for collimating UV light emitted from an LED with large divergent angle. ***Optik***, *181*(March 2018), 1039–1048. https://doi.org/10.1016/j.ijleo.2018.12.057

LEELADHAR; RATURI, Parul; SINGH, J. P. Sunlight-driven eco-friendly smart curtain based on infrared responsive graphene oxide-polymer photoactuators. **Scientific Reports,** v. 8, n. 1, p. 1–9, 2018. Available in: <http://dx.doi.org/10.1038/s41598-018-21871-3>.

LEVENSPIEL. **Chemical reaction Engineering.** 3rd ed. John Wiley & Sons, Inc., 1999.

LEWIS, Nathan S.; NOCERA, Daniel G. Powering the planet: Chemical challenges in solar energy utilization. **Proceedings of the National Academy of Sciences of the United States of America,** v. 103, n. 42, 2006.

LIU, Cheng *et al.* Luminescent solar concentrators fabricated by Ultraviolet not Visible light. **International Journal of Photoenergy,** v. 2014, p. 1–6, 2014.

M. ZELLER. **Application of organic photoredox catalysis in new reaction,** 2016.

MANZANO CHÁVEZ, Lisset. **Optimization of a Luminescent Solar Concentrator Simulation and application in PowerWindow design.** 2017. Available in: <http://repository.tudelft.nl/.>.

MARTINEZ, Glaucia R. *et al.* Synthesis of a hydrophilic and non-ionic anthracene derivative, the N,N′-di-(2,3-dihydroxypropyl)-9,10-anthracenedipropanamide as a chemical trap for singlet molecular oxygen detection in biological systems. **Tetrahedron,** v. 62, n. 46, p. 10762–10770, 2006.

MATSUSHITA, Yoshihisa *et al.* Recent progress on photoreactions in microreactors*. **Pure Appl. Chem,** v. 79, n. 11, p. 1959–1968, 2007.

MCGEE, H. A. **Molecular Engineering.** McGraw-Hill, 1991.

MEINARDI, Francesco *et al.* Large-area luminescent solar concentrators based on Stokes-shift-engineered nanocrystals in a mass-polymerized PMMA matrix. **Nature Photonics,** v. 8, n. 5, p. 392–399, 2014.

MEINARDI, Francesco; BRUNI, Francesco; BROVELLI, Sergio. Luminescent solar concentrators for building-integrated photovoltaics. **Nature Reviews Materials,** v. 2, p. 1–9, 2017. Available in: <http://dx.doi.org/10.1038/natrevmats.2017.72>.

MENG, Qing-yuan *et al.* A Cascade Cross-Coupling Hydrogen Evolution Reaction by Visible Light Catalysis. **Journal of the American Chemical Society,** p. 19052–19055, 2013.

MEYER, Susann *et al.* Photosensitized oxidation of citronellol in microreactors. **Journal of Photochemistry and Photobiology,** v. 186, p. 248–253, 2007.

MO, Qi *et al.* Analytic ray curve tracing for outdoor sound propagation. **Applied Acoustics,** v. 104, p. 142–151, 2016.

MORAITIS, P.; SCHROPP, R. E.I.; VAN SARK, W. G.J.H.M. Nanoparticles for Luminescent Solar Concentrators - A review. **Optical Materials,** v. 84, n. March, p. 636–645, 2018. Available in: <https://doi.org/10.1016/j.optmat.2018.07.034>.

Mouedden, Y. El. (2016). Lifetime and efficiency improvement of organic luminescent solar concentrators for photovoltaic applications. *Edith Cowan University*, ***Thesis*.** Retrieved from https://ro.ecu.edu.au/theses/1779

MUKAMEL, Shaul. Trees to trap photons. **Nature,** v. 388, p. 425–427, 1997.

NARAYANAM, Jagan M R; TUCKER, Joseph W; STEPHENSON, Corey R J. Electron-

Transfer Photoredox Catalysis: Development of a Tin-Free Reductive Dehalogenation Reaction. **JACS Communications,** v. 2, n. eq 2, p. 8756–8757, 2009.

NICHOLLS, T. P., Leonori, D., & Bissember, A. C. (2016). Applications of visible lightphotoredox catalysis to the synthesis of natural products and related compounds. **Natural products reports**, *33*(11), 1248–1254. https://doi.org/10.1039/C6NP00070C

NOËL, Timothy. A personal perspective on the future of flow photochemistry. **Journal of Flow Chemistry,** v. 7, n. 3–4, p. 87–93, 2017. Available in: <http://www.akademiai.com/doi/10.1556/1846.2017.00022>.

O-CHAROEN, Sirimon; SRIVANNAVIT, Onnop; GULARI, Erdogan. Simulation and Visualization of Flow Pattern in Microarrays for Liquid Phase Oligonucleotide and Peptide Synthesis. **Biotechnol. Prog.,** p. 755–761, 2007.

OBAMA, Barack. The irreversible momentum of clean energy. **Science,** v. 355, n. 6321, p. 126–129, 2017. Disponível em: <http://www.sciencemag.org/lookup/doi/10.1126/science.aam6284>.

ODIBA *et al.* Computational Fluid Dynamics in Microreactors Analysis and Design: Application to Catalytic Oxidation of Volatile Organic Compounds. **Chemical Engineering & Process Technology,** v. 7, n. 3, 2016.

OELGEMÖLLER, Michael. Solar Photochemical Synthesis: From the Beginnings of Organic Photochemistry to the Solar Manufacturing of Commodity Chemicals. **Chemical Reviews,** 2016.

OELGEMÖLLER, M. Highlights of Photochemical Reactions in Microflow Reactors. **Chemical Engineering and Technology,** v. 35, n. 7, p. 1144–1152, 2012.

OELGEMÖLLER, Michael; JUNG, Christian; MATTAY, Jochen. Green photochemistry: Production of fine chemicals with sunlight*. **Pure Appl. Chem.,** v. 79, n. 11, p. 1939–1947, 2007.

PITRE, Spencer P. *et al.* Visible-Light Actinometry and Intermittent Illumination as Convenient Tools to Study Ru(bpy)3Cl2Mediated Photoredox Transformations. **Scientific Reports,** v. 5, n. November, p. 1–10, 2015. Available in: <http://dx.doi.org/10.1038/srep16397>.

PITRE, Spencer P; MCTIERNAN, Christopher D; SCAIANO, Juan C. Understanding the Kinetics and Spectroscopy of Photoredox Catalysis and Transition-Metal-Free Alternatives. **Accounts of Chemical Research,** 2016.

Pohlmann, B., Scharf, H. D., Jarolimek, U., & Mauermann, P. (1997). Photochemical production of fine chemicals with concentrated sunlight. **Solar Energy**, *61*(3), 159168. https://doi.org/10.1016/S0038-092X(97)00043-1

RAVELLI, Davide; FAGNONI, Maurizio; ALBINI, Angelo. Photoorganocatalysis. What for?. **Chem. Soc. Rev.,** p. 97–113, 2013.

RAZEGHIFARD, Reza. **Natural and artificial photosynthesis.** 2013.

REHMAN, Naveed. Optical-irradiance ray-tracing model for the performance analysis and optimization of a single slope solar still. **Desalination,** v. 457, n. October 2018, p. 22–31, 2019. Available in: <https://doi.org/10.1016/j.desal.2019.01.026>.

RICHARDS, B. S., & McIntosh, K. R. (2006). Ray-Tracing Simulations of Luminescent Solar Concentrators Containing Multiple Luminescent Species. ***21st European Photovoltaic Solar Energy Conference***, (September), 185–188.

RONCALI, J; GARNIER, F. Photon-transport properties of luminescent solar concentrators : analysis and optimization. **Applied Optics,** v. 23, n. 16, p. 2809–2817, 1984.

SANSANIWAL, Sunil Kumar; SHARMA, Vashimant; MATHUR, Jyotirmay. Energy and exergy analyses of various typical solar energy applications: A comprehensive review. **Renewable and Sustainable Energy Reviews,** v. 82, n. May 2017, p. 1576–1601, 2018. Available in: <https://doi.org/10.1016/j.rser.2017.07.003>.

SANTANA, Harrson S; SILVA, João L; TARANTO, Osvaldir P. Development of microreactors applied on biodiesel synthesis: From experimental investigation to numerical approaches. **Journal of Industrial and Engineering Chemistry,** v. 69, p. 1–12, 2019. Available in: <https://doi.org/10.1016/j.jiec.2018.09.021>.

SARK, Wilfried G.J.H.M. Van *et al.* Luminescent Solar Concentrators - A review of recent results. **Optics Express,** v. 16, n. 26, p. 21773, 2008. Available in: <https://www.osapublishing.org/oe/abstract.cfm?uri=oe-16-26-21773>.

SCHOLES, Gregory D. *et al.* Lessons from nature about solar light harvesting. **Nature Chemistry,** v. 3, n. 10, p. 763–774, 2011. Available in: <http://dx.doi.org/10.1038/nchem.1145>.

SCHRECENGOST, Jonathon R. *et al.* Increasing the area of a white scattering background can increase the power output of a luminescent solar concentrator. **Solar Energy,** v. 170, n. February, p. 132–137, 2018. Available in: <https://doi.org/10.1016/j.solener.2018.05.022>.

SCHULTZ, Danielle M.; YOON, Tehshik P. Solar synthesis: Prospects in visible light photocatalysis. **Science,** v. 343, n. 6174, 2014.

SEEBERGER, Peter H. Highly Efficient Continuous Flow Reactions Using Singlet Oxygen as a “ Green ” Reagent. **Organic Letters,** n. 11, p. 11–14, 2011.

SHI, Lei; XIA, Wujiong. Photoredox functionalization of C – H bonds adjacent to a nitrogen atom. **Chem. Soc. Rev.,** p. 7687–7697, 2012.

SHVYDKIV, Oksana. **Microphotochemistry – a New Resources-Efficient Synthesis Tool Approach.** 2012.

SKUBI, Kazimer L; BLUM, Travis R; YOON, Tehshik P. Dual Catalysis Strategies in Photochemical Synthesis. **Chemical Reviews,** 2016.

SLOOFF, L H *et al.* A luminescent solar concentrator with 7 . 1 % power conversion efficiency. **Rapid Research Letters,** v. 259, n. 6, p. 257–259, 2008.

SUMNER, Ryan *et al.* Analysis of Optical Losses in High-Efficiency CuInS2-Based Nanocrystal Luminescent Solar Concentrators: Balancing Absorption versus Scattering. **The Journal of Physical Chemistry,** 2017.

SYNOPSYS. **Core Module User 's Guide**. June, 2018a.

SYNOPSYS. I**llumination Module User's Guide**. June, 2018b.

TU, Jiyuan; YEOH, Guan-Heng; LIU, Chaoqun. **Computational Fluid Dynamics.** 2018.

TUMMELTSHAMMER, Clemens. **Pathways to a brighter luminescent solar concentrator.** London, 2016.

VADAS, S L; FRITTS, D C. Reconstruction of the gravity wave field from convective plumes via ray tracing. **Annales Geophysicae,** p. 147–177, 2009.

VAN SARK, Wilfried G J H M. Luminescent solar concentrators - A low cost photovoltaics alternative. **Renewable Energy**, v. 49, p. 207–210, 2013. Available in: <http://dx.doi.org/10.1016/j.renene.2012.01.030>.

Vishwanathan, B., Reinders, A. H. M. E., de Boer, D. K. G., Desmet, L., Ras, A. J. M., Zahn, F. H., & Debije, M. G. (2015). A comparison of performance of flat and bent photovoltaic luminescent solar concentrators. **Solar Energy**, *112*, 120–127. https://doi.org/10.1016/j.solener.2014.12.001

WASSERBERG, D. **Triplet States – Triplet Fates Phosphorescence and Energy Transfer in Functional Molecules.** 2006.

WELTY, James R. *et al.* **Fundamentals of Momentum, Heat, and Mass Transfer.** 5th editio ed. John Wiley & Sons, Inc., 2008.

WIELAND, Eric. **Rapid prototyping of Luminscent Solar Concetrator based**

photoreactors via 3D printing. 2016.

WU, Wenxuan *et al.* Hybrid solar concentrator with zero self-absorption loss. **Solar Energy,** v. 84, n. 12, p. 2140–2145, 2010.

XUAN, Jun; XIAO, Wen-jing. Visible-Light Photoredox Catalysis. **Angewandte Minireviews,** p. 6828–6838, 2012.

YADAV, N. G. *et al.* Impact of collected sunlight on ZnFe2O4nanoparticles for photocatalytic application. **Journal of Colloid and Interface Science,** v. 527, p. 289–297, 2018. Available in: <https://doi.org/10.1016/j.jcis.2018.05.051>.

YANG, W. M. *et al.* Impact of emulsion fuel with nano-organic additives on the performance of diesel engine. **Applied Energy,** v. 112, p. 1206–1212, 2013.

YOSHIDA, Jun-ichi; KIM, Heejin; NAGAKI, Aiichiro. Green and Sustainable Chemical Synthesis Using Flow Microreactors. **Chem. Sus. Chem,** v. 8510, p. 331–340, 2011.

ZHAO, Fang; CAMBIÉ, Dario; HESSEL, Volker; *et al.* Real-time reaction control for solar production of chemicals under fluctuating irradiance. **Green Chemistry,** v. 20, n. 11, p. 2459–2464, 2018b.

ZHAO, Fang; CAMBIÉ, Dario; JANSE, Jeroen; *et al.* Scale-up of a Luminescent Solar Concentrator-Based Photomicroreactor via Numbering-up. **ACS Sustainable Chemistry and Engineering,** v. 6, n. 1, p. 422–429, 2018a.

ZOLLERS, Michael. **Phosphor Modeling in LightTools.** 2018.

APPENDIX A – Supplementary material for the CFD simulation

Figure A1 - Determination of the specific rate constant (k) for different tip powers according to the experimental data.

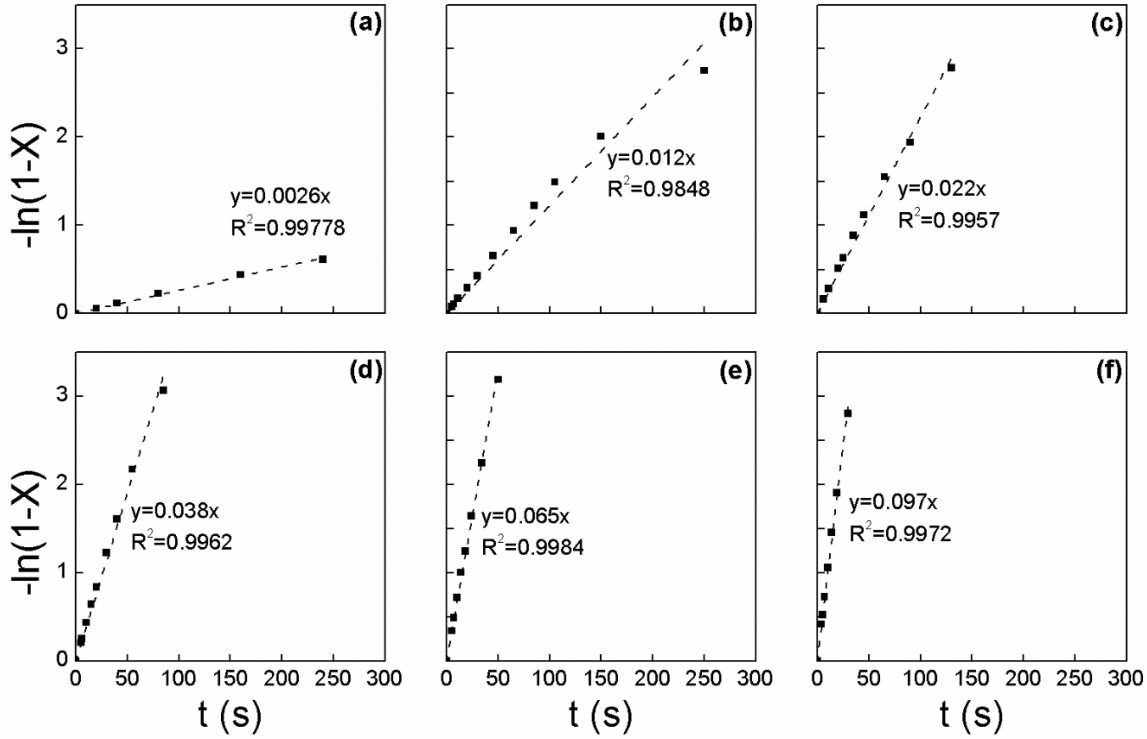

(a) $P_1 = 0.010\ W$; (b) $P_2 = 0.058\ W$; (c) $P_3 = 0.093\ W$; (d) $P_4 0.17\ W$;
(e) $P_5 = 0.30\ W$; (f) $P_6 = 0.48\ W$.

Table A1 - Experimental data provided by the Noël Research Group, Eindhoven University of Technology.

A		**B**		**C**		**D**		**E**		**F**	
P=0.010 W		P=0.058 W		P=0.093 W		P=0.17 W		P=0.30 W		P=0.48 W	
t	X	t	X	t	X	t	X	t	X	t	X
(s)	(%)	(s)	(%)	(s)	(%)	(s)	(%)	(s)	(%)	(s)	(%)
0	0	0	0	0	0	0	0	0	0	0	0
20	5.7	5	7.7	6	15.0	5	18.9	5	29.1	4	34.3
40	10.9	7	10.6	11	24.8	6	22.7	7	38.9	5	40.9
80	20.4	11	16.0	20	39.9	10	35.4	10	51.4	7	51.9
160	35.6	20	25.6	25	46.9	15	47.7	14	63.4	10	65.3
240	45.8	30	34.6	35	58.6	20	57.0	18	71.3	14	76.8
		45	48.1	45	67.4	30	70.8	24	80.8	19	85.1
		65	60.9	65	78.8	40	80.1	34	89.4	30	94.0
		85	70.6	90	85.7	55	88.7	50	95.9		
		105	77.5	130	93.8	85	95.4				
		150	86.6								
		250	93.7								

Light Source: white LED strip, powered by a power source

P = output of the LED in the range of 350-700 nm (light flux reaching the LSC-PM top surface)

Reaction mixture: DPA 0.1 mM and MB 0.2 mM

G.C.I Code run in the software GNU Octave 4.2.1

```
clear all;

#####GCI de um unico ponto (variavel   global)#####

%================================3D====================
%==============================MALHAS==================
%Numero de elementos:
N1=766544; % MalhaFina
N2=43290;  % MalhaMedia
N3=1790;   % MalhaGrossa
%=========================================================
h1=(1/N1)^(1/3);
h2=(1/N2)^(1/3);
h3=(1/N3)^(1/3);

r21=h2/h1
r32=h3/h2
%============================VARIAVEL====================
NomeDaVariavel="DPA Conversion(%)";
f1=0.08776; %(MalhaFina)
f2=0.08760; %(MalhaMedia)
f3=0.08723; %(MalhaGrossa)
%=========================================================
e32=f3-f2;
e21=f2-f1;

function y=funp(x,e32,e21,r32,r21)
       s=1*sign(e32/e21);
       q=log(((r21^x)-s)/((r32^x)-s));
       y=(abs(log(abs(e32/e21))+q)/(log(r21)))-x;
endfunction
```

```
p=fzero(@(x) funp(x,e32,e21,r32,r21),15)%%%%%

%f_ex32=((r32^p)*f2-f3)/((r32^p)-1)
f_ex21=((r21^p)*f1-f2)/((r21^p)-1)

%E_a32=abs((f2-f3)/f2)
E_a21=abs((f1-f2)/f1)

%E_ex32=abs((f_ex32-f2)/f_ex32)
E_ex21=abs((f_ex21-f1)/f_ex21)

%GCI32=(1.25*E_a32/((r32^p)-1))*100
GCI21=(1.25*E_a21/((r21^p)-1))*100
GCI32=GCI21*r21**p
%============================GRAFICO==================
xnumber=[0 1/N1 1/N2 1/N3];
ynumber=[f_ex21 f1 f2 f3];
splynumber   =   interp1   (xnumber,ynumber,[0:1/(50*N1):1/N3],
"cubic");
plot(xnumber,ynumber,"xb;;",...
         [0:1/(50*N1):1/N3],splynumber,"-r;;")
xlabel("1/N");
A=(1/N3)+0.05*(1/N3)
xlim([-1e-10,A]);
ylabel(NomeDaVariavel);
```

APPENDIX B – Supplementary material for ray-tracing simulation

Table B1 – MFP dependence of the system.

MFP (mm)	Incident power (W)	Absorbed power (W)	Nº of samples	Output power (W)	Nº of samples
0.1	1.9754	0.0688	4914258	0.0034	11429
0.2	1.9717	0.0795	4861786	0.0066	21279
0.3	1.9581	0.0902	4745804	0.0094	28094
0.4	1.9376	0.0991	4602783	0.0116	32496
0.5	1.9124	0.1054	4457620	0.0135	35870
0.6	1.8847	0.1097	4321235	0.0150	38298
0.7	1.8570	0.1129	4199718	0.0162	40167
0.8	1.8294	0.1150	4090295	0.0170	41438
0.9	1.8025	0.1163	3991951	0.0177	42389
1.0	1.7771	0.1171	3904270	0.0183	43133
2.0	1.5874	0.1116	3351859	0.0197	43981
3.0	1.4739	0.1018	3066784	0.0188	41218
4.0	1.3985	0.0931	2886967	0.0179	38793
5.0	1.3443	0.0860	2760523	0.0169	36409
6.0	1.3029	0.0799	2666220	0.0158	34117
7.0	1.2704	0.0751	2592428	0.0150	32204
8.0	1.2442	0.0711	2533336	0.0141	30345
9.0	1.2224	0.0676	2484685	0.0135	28962
10	1.2043	0.0646	2444372	0.0122	27456
15	1.1447	0.0543	2313030	0.0105	22300
20	1.1114	0.0486	2240343	0.0088	18606

ATTACHMENT

Table A – Irradiation data for Eindhoven, The Netherlands.

Date	Time	GHI avg	DNI avg	Direct component
22/09/2017	10:00:00	466.415	424.254	299.836
22/09/2017	10:01:00	477.965	415.677	295.106
22/09/2017	10:02:00	466.273	323.78	230.897
22/09/2017	10:03:00	430.339	268.129	192.061
22/09/2017	10:04:00	410.002	215.535	155.069
22/09/2017	10:05:00	442.642	276.964	200.136
22/09/2017	10:06:00	376.529	148.131	107.504
22/09/2017	10:07:00	310.757	39.98	29.139
22/09/2017	10:08:00	309.491	58.877	43.095
22/09/2017	10:09:00	298.334	57.302	42.126
22/09/2017	10:10:00	272.423	24.258	17.908
22/09/2017	10:11:00	266.746	19.164	14.208
22/09/2017	10:12:00	260.526	12.727	9.474
22/09/2017	10:13:00	270.364	25.572	19.117
22/09/2017	10:14:00	283.587	41.599	31.223
22/09/2017	10:15:00	297.845	65.754	49.557

Reference: Zhao *et al.* (2018).

Latitude: 51.26 degrees north
Longitude -5.29 degrees east
Time zone offset from GMT: 1 h
Zero azimuth in south